Download PDF: 15.12.2025

ETH-Bibliothek Zürich, E-Periodica, https://www.e-periodica.ch

Working Session

Innovative Design against Vibration of Tall Buildings

Papers

Leere Seite

Blank page

Page vide

Deformation Behaviour of Base-Isolated Buildings in Near-Fault Earthquake

Masayoshi NAKASHIMA
Assoc. Prof.
Kyoto Univ.
Kyoto, Japan

Masayoshi Nakaashima received his B.S. and M.S. from Kyoto Univ., Japan and Pd.D. from Lehigh Univ., USA. He has been involved with analysis and seismic design of steel buildings structures and development of experimental techniques for earthquake response simulation.

Summary

Response behavior of base-isolated buildings subjected to near-fault earthquakes was examined. Recorded, synthesized, and simplified ground motions were used in the analysis. It was found that (1) a large ground motion component appearing at a particular time tends to control the maximum deformation and (2) dynamic amplification and increase in ductility demand is most significant when the natural period of buildings under smaller vibration is 0.4 to 0.8 times the period of a large ground motion component.

1. Introduction

The 1995 Hyogoken-Nanbu (Kobe) Earthquake revealed much damage to modern building structures [1]. Although many of those damaged escaped from collapse, their functionality was severely impaired, resulting in significant loss in capital. Since that experience, importance on the control of functionality (in addition to collapse prevention) has been emphasized greatly. One solution toward this end is considered as "base-isolation." Japan has a history of construction of base-isolated buildings for nearly fifteen years [2], but the construction was limited, remaining about a dozen new base-isolated buildings annually. After the Kobe Earthquake, the construction has grown significantly, and more than 150 new base-isolated buildings were built for a single year of 1997 [3]. On the other hand, ground motion specialists address the possibility of a very large pulse-like ground motion in near-fault regions, particularly in the direction perpendicular to the fault [4,5] and warn that such large ground motion can induce very large deformations to structures with long natural periods such as base-isolated buildings. On one hand, construction of base-isolated buildings has grown with the belief that they are effective in damage control against large earthquakes; on the other hand, base-isolation may be useless for near-fault earthquakes; this rather conflicting argument has to be resolved. To provide some information on this issue, numerical response analysis was carried out for base-isolated buildings represented as SDOF systems, with the type of ground motion, type of hysteretic behavior, and natural period as major variables, and their effects on the response were examined. To understand the basic behavior of base-isolated buildings subjected to near-fault earthquakes, the ground motion was simplified as a one-cycle sinusoidal ground motion (acceleration), and the response of SDOF systems subjected to the motion was investigated in terms of the dynamic amplification of maximum deformations.

2. Numerical Analysis

In base-isolated buildings, it is a common practice to make the base-isolation devices much more flexible (in the horizontal direction) than the super-structure, and the super-structure would not go beyond its elastic limit. Therefore, an SDOF representation (Fig.1) is reasonable, with the super-structure assumed to be completely rigid and flexibility provided only by the base-isolation devices. Thirty eight base-isolated buildings previously designed were surveyed for the hysteretic behavior of their base-isolation devices. (Necessary information was obtained from the data presented in [3].) In all buildings, the maximum deformation under ambient and small vibrations was limited to 5 to 10% in terms of the shear strain (γ) of the rubber bearings, and the maximum deformation under large earthquakes (approximately 0.5 m/s in the maximum ground velocity) was limited to $\gamma = 150 - 200\%$. The equivalent natural period (estimated based upon the secant stiffness) of base-isolated buildings equipped with rubber bearings with lead dampers (14 buildings surveyed) ranged from 1.2 to 1.8 sec for a deformation corresponding to $\gamma = 15 - 20\%$, and the tangential stiffness under large deformations (corresponding to $\gamma = 100 - 300\%$) was about 10 to 15 % of the secant stiffness at $\gamma = 15 - 20\%$. The equivalent natural period of base-isolated buildings equipped with high damping rubber bearings (14 buildings surveyed) ranged from 1.1 to 1.7 sec for a deformation corresponding to $\gamma = 20 \%$, and the tangential stiffness under large deformations was about 20 - 25 % of the secant stiffness at $\gamma = 20\%$. The equivalent natural period of base-isolated buildings equipped with a combination of natural rubber bearings and lead and steel dampers (10 buildings surveyed) ranged from 1.7 to 1.9 sec for a deformation corresponding to $\gamma = 10 \%$ (at which steel dampers were expected to yield), and the tangential stiffness for large deformations was about 15 - 20% of the secant stiffness at $\gamma = 10\%$. From these observations, the hysteresis of base isolation devices can reasonably be approximated to be bilinear (Fig.1), with the first stiffness corresponding to the equivalent natural period of 1.0 - 2.0 sec and the second stiffness equal to 10 - 25 % of the first stiffness. Considering these values, bilinear SDOF systems having the elastic natural period
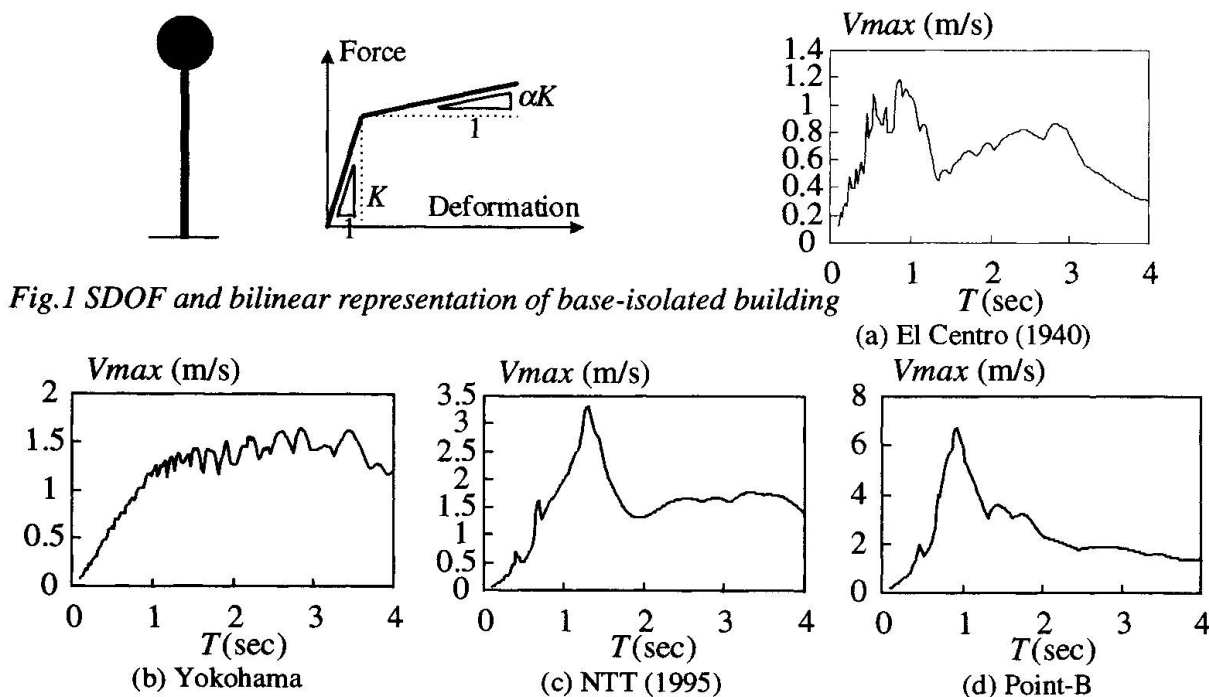

Fig.1 SDOF and bilinear representation of base-isolated building

(a) El Centro (1940)

(b) Yokohama

(c) NTT (1995)

(d) Point-B

Fig.2 Elastic pseudo velocity spectra of ground motions analyzed

(T) of 1.0, 1.5 and 2.0 sec and the second stiffness that is 15 and 25 % of the initial stiffness were analyzed. The following four ground motions were selected: El Centro NS (1940), Yokohama (1995), NTT (1995), and Point-B(1996). El Centro record was selected as the basis of comparison because the record has been used extensively for earthquake response investigations. Yokohama (1995) is a synthesized motion having almost a constant pseudo ground velocity over a large range, developed for the simulation of ocean-ridge earthquakes. NTT (1995) is a ground motion recorded during the Kobe Earthquake, and Point-B is a synthesized motion that simulated the ground motion at downtown Kobe during the Kobe Earthquake [6] The last two motions were selected as representatives of near-fault ground motions. The elastic pseudo velocity ($Vmax$) spectra of these four motions are shown in Fig.2.

Figure 3 shows examples of input and dissipated energies in terms of the equivalent velocities (VE and VP), and Fig.4 shows the maximum deformations ($Dmax$), ratios of the maximum plastic deformation relative to the cumulative plastic deformation [$(\mu - 1)/\eta$], and the number of inelastic excursions (N). These figures are for the second stiffness equal to 25 % of the initial stiffness. In the figure, f indicates the yield force, defined as the yield force relative to the maximum force exerted if the system would respond only elastically under the same ground motion. The energy behavior is summarized as follows. In El Centro and Yokohama both input and dissipated energies are relatively constant regardless of the yield force and do not change significantly for the three natural periods (1.0, 1.5, and 2.0 sec). This supports the energy constant concept advocated in [7]. In NTT and Point-B the energy terms fluctuate with respect to the yield force and are different significantly for the three natural periods. According to Fig.4(a), the maximum deformation does not change so significantly with respect to the yield force in El Centro and Yokohama, supporting the maximum deformation constant rule [8], whereas the maximum deformation in NTT and Point-B change significantly with the yield force. Figure 4(b) shows that the ratio of maximum plastic deformation to cumulative plastic deformation is largest in NTT, followed by Point-B, El Centro, and Yokohama. The larger ratio means that the energies exerted and dissipated for one large response cycle is more significant relative to the total input and dissipated energies. This suggests that the response is more dominated by a large, single shock rather than accumulated by smaller but multiple shocks. This statement is supported by Fig.4(c), in which the number of inelastic excursions is significantly smaller in NTT and Point-B. It was also observed that in NTT and Point-B the maximum deformation was achieved around the same time regardless of the yield force and natural period, indicating that the maximum deformation was induced by a large ground motion component appearing at a particular time, whereas in El Centro and Yokohama the time at attainment of the maximum deformation varied from case to case. In summary, the response behavior for near-fault earthquakes (represented by NTT and Point-B) is characterized as follows. (1) The maximum deformation tends to be induced by a large ground motion
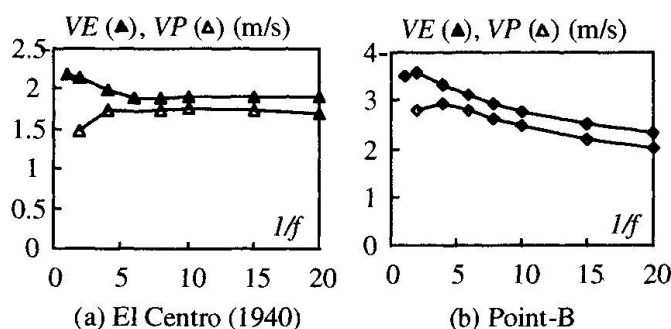

(a) El Centro (1940)   (b) Point-B

Fig.3 Input and dissipated energies of SDOF bilinear systems (T=1.5 sec)

(a) Maximum Deformation

(b) Ratio of Maximum Plastic Deformation to Cumulative Plastic Deformation

(c) Number of Inelastic Excursions

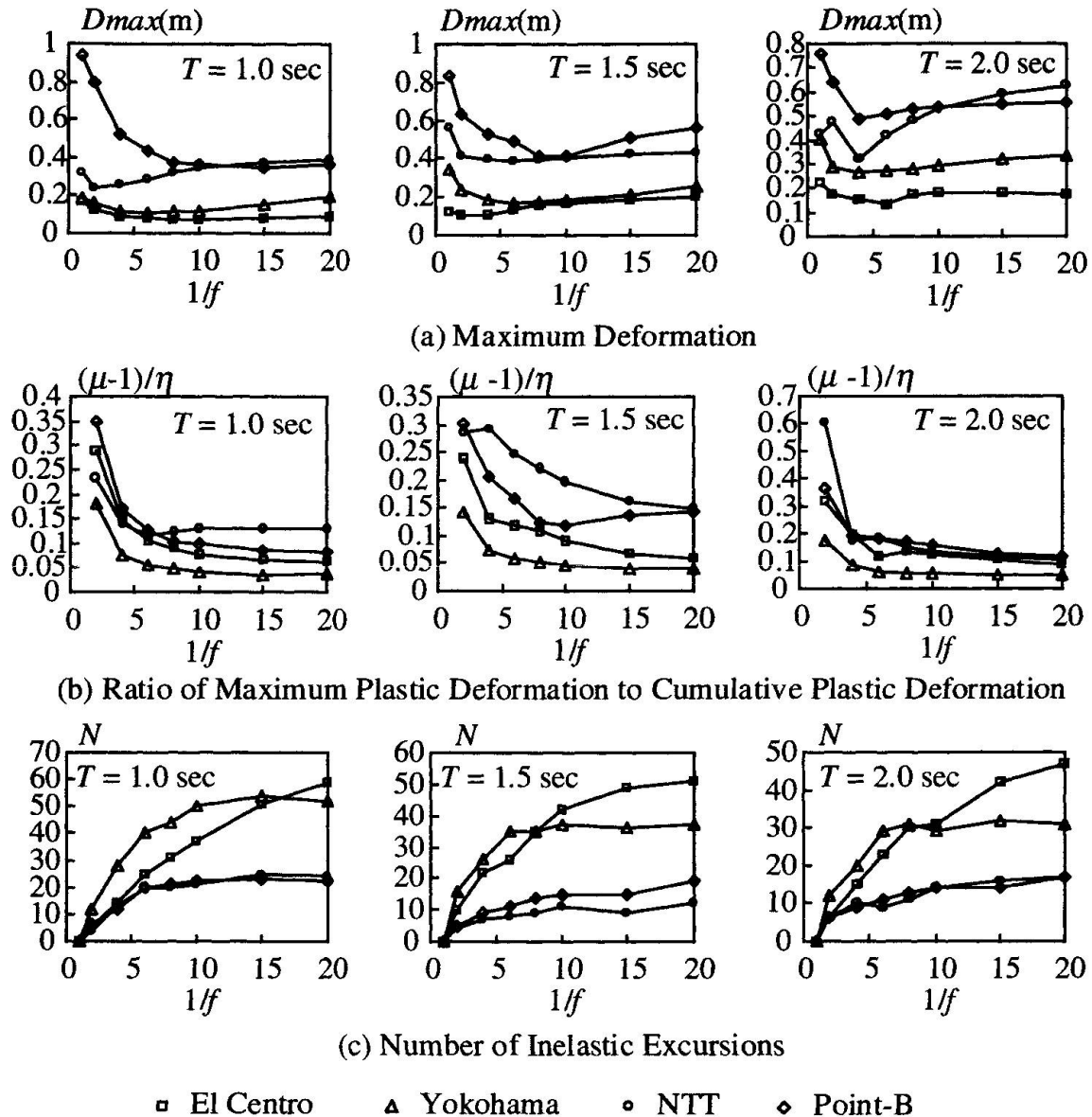□ El Centro   ▲ Yokohama   ○ NTT   ◇ Point-B

Fig.4 Response characteristics of bilinear SDOF systems

component appearing at a particular time, (2) the input and dissipated energies vary significantly with respect to the yield force and natural period, leading the energy constant concept less certain, and (3) the maximum deformation is dependent much on the yield force, making the constant maximum deformation rule less applicable.

3. Behavior of SDOF Systems Subjected to One-Cycle Sinusoidal Motion

In reference to the above discussion, it is interesting to examine how the system would behave under a large ground motion component. As a most simplified form of such motion, one cycle sinusoidal ground motion was considered (Fig.5), and the response of bilinear SDOF systems subjected to the motion was obtained.. Figure 6 shows the maximum deformation in terms of the ductility ratio (μ), defined as the maximum deformation relative to the elastic limit rotation, for various natural periods (T/Te) and the yield force (f). Here, Te is the period of the sinusoidal ground motion, and the yield force f is defined as the yield force relative to the maximum force exerted for the equivalent elastic system subjected to one-half cycle sinusoidal motion. Figure
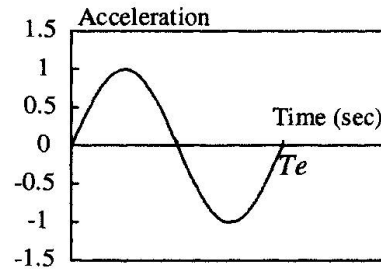
1.5 Acceleration
1
0.5
0 Time (sec)
-0.5 /Te
-1
-1.5

Fig.5 One-cycle sinusoidal ground motion analyzed

μ+(positive excursion)

60
50   1/f = 10
40
30   1/f = 8
20   1/f = 6
10   1/f = 4
0
0   1/f = 2   1   2   3   4
                    T/Te

(a) ductility ratio
for positive excursion

μ-(negative excursion)

70
60   1/f = 10
50
40   1/f = 8
30
20   1/f = 6
10   1/f = 4
0
0   1/f = 2   1   2   3   4
                    T/Te

(b) ductility ratio
for negative excursion

μ-/ μ +

2
1.8
1.6
1.4
1.2
1
0.8
0.6
0.4
0.2
0
0   1   2   3   4
              T/Te
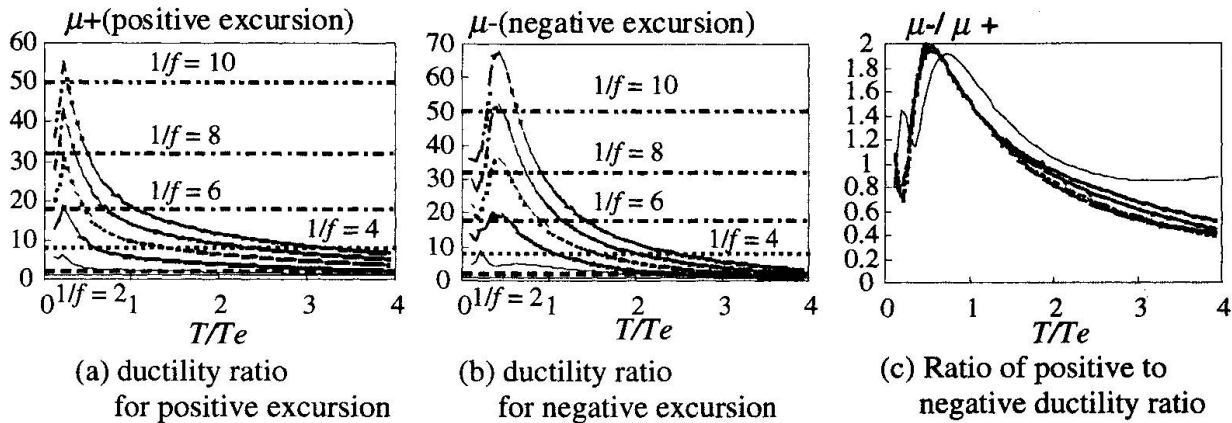
(c) Ratio of positive to
negative ductility ratio

*Fig.6 Response characteristics of bilinear SDOF systems subjected
to one-cycle sinusoidal ground motion*

6(a) is the maximum deformation obtained for the positive excursion, Fig.6(b) the maximum deformation for the negative excursion, and Fig. 6(c) is the ratio of the negative maximum to the positive maximum, indicating that the maximum deformation is achieved in the negative excursion for $T/Te \leq 2.0$. Most notable is that the ductility ratio is largest around $T/Te = 0.4$ and significantly reduces with the increase of T/Te. In reference to the definition of f, this figure provides an answer to the following question; i.e. if the yield force is reduced to f times the maximum force exerted in the elastic system, how much ductility should we consider? Figure 6 also shows the ductility ratios estimated based on the energy equivalent rule [8]. The obtained ductility ratios are much larger than those estimated for about $T/Te = 0.4$. Figure 7 shows another form of ductility ratio, this time the maximum deformation is normalized by the maximum deformation if the system receives the motion statically, thus enabling the direct comparison of maximum deformation. When $T/Te \leq 1.0$, the difference is significant with respect to the yield force, indicating that the maximum deformation rule is less reliable. These observations reveals that dynamic amplification and increase in ductility demand is very large for $T/Te = 0.4 - 0.8$. Earlier discussion demonstrated that the equivalent natural period of previously designed base-isolated buildings ranged from 1.0 to 2.0 sec for small deformations, which means that if a near-fault ground motion contains a large component having a period of 1.25 (= 1/0.8) sec or more, base-isolated buildings would sustain very large dynamic amplification.

A separate study is underway to derive approximate closed-form equations for estimating the ductility ratio (μ) of bilinear SDOF systems subjected to one cycle sinusoidal ground motion. The equations are applicable for $0.5 \leq T/Te \leq 2.0$, the range of most importance in terms of dynamic amplification and increase in ductility. In formulating the equations, the deformation shape was assumed to be sinusoidal, and the energy balance between the input and absorbed
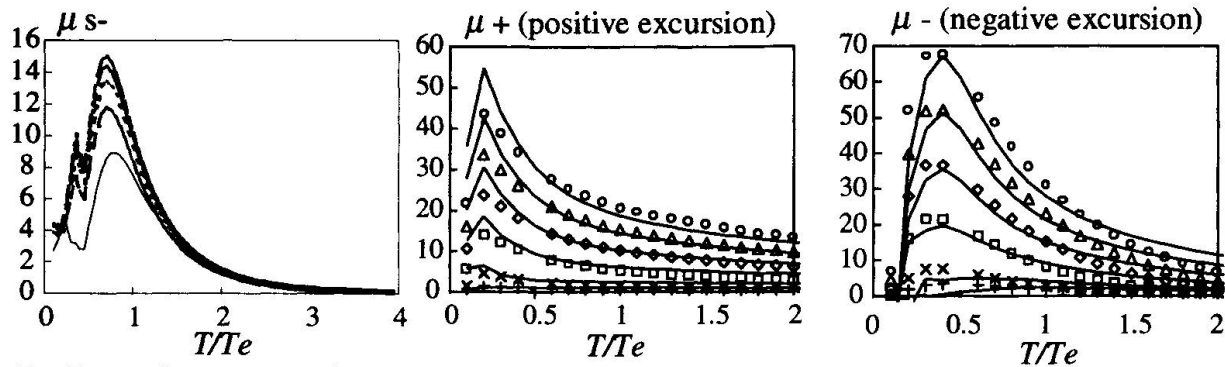
Fig.7 Ductility ratios with respect (a) ductility ratio (b) ductility ratio
to static deformation for positive excursion for negative excursion

Fig.8 Comparison between estimated and analyzed ductility ratios

energies was considered [9]. Figure 8 shows comparison between the estimated and numerically ductility ratios, demonstrating reasonable agreement between the two.

4. Conclusion

Response behavior of base-isolated buildings subjected to near-fault earthquakes was examined. The behavior was found to be characterized such that: (1) a large ground motion component appearing at a particular time tends to control the maximum deformation and (2) energy constant concept, energy equivalent rule, and maximum deformation constant rule are less applicable. Response behavior when subjected to one-cycle sinusoidal ground motion was examined. Dynamic amplification and increase in ductility demand was found to be most significant when the equivalent natural period of buildings in small vibrations is 0.4 to 0.8 times the period of the motion.

References

[1] The Architectural Institute of Japan (AIJ) (1995). English Edition of Preliminary Reconnaissance Report of the 1995 Hyogoken-Nanbu Earthquake, 215pp.

[2] Menshin (1996). Japan Society of Seismic Isolation, No.16, pp.20-31.

[3] Building Letters (1996). The Building Center of Japan, No.348 to 359.

[4] Hall, J., et al. (1995). Near-source ground motion and its effects on flexible buildings, Earthquake Spectra, Vol.11, pp.569-605.

[5] Heaton, T. H., et al. (1995). Response of high-rise and base-isolated buildings to a hypothetical Mw 7.0 blind thrust earthquake, Science, Vol.267, pp.206-211

[6] Hayashi, Y. and Kawase. H. (1996). Strong motion evaluation in Chuo Ward, Kobe, during the Hyogoken-Nanbu Earthquake of 1995, Journal of Structural and Construction Engineering, the Architectural Institute of Japan, No.481, pp.37-46 (in Japanese).

[7] Akiyama, H. (1985). Earthquake-resistant Limit-State Design of Buildings, University of Tokyo Press, Tokyo.

[8] Newmark N. M. and Hall, W. J. (1975). Earthquake Spectra and Design, Earthquake Engineering Research Institute.

[9] Nakashima, M. (1998). Prediction of Maximum Deformation of Base-Isolated buildings subjected to pulse-like ground motions, Report to Grant-in-Aid for Scientific Research on Mitigation of Urban Disasters by Near-Field Earthquakes, Ministry of Education, Japan, 87pp.

Active Structural Seismic Control Including Ground Rigidity Effects

Jinmin ZAI
Prof.
Nanjing Arch. & Civil Eng. Inst.
Nanjing, China

Guoxing CHEN
Prof.
Nanjing Arch. & Civil Eng. Inst.
Nanjing, China

Dong YANG
PhD
Nanjing Arch. & Civil Eng. Inst.
Nanjing, China

Dajun DING
Prof.
Southeast Univ.
Nanjing, China

Summary

The characteristics of active structural control, namely active pulse control (APC) and active anchor rope control (AARC), on the six-storey frame structure considering soil-structure interaction (SSI) effects were examined. The results show that the effect of APC is better and the AARC may take no effect at all on soft ground due to the SSI effects. The APC force can be greatly reduced by 1/3 to 1/2 when the SSI effects are considered in comparison with the result of rigid-foundation assumption. The extent of control force reduced will be increased as the soil becomes softer. It seems unnecessary in some conditions to use active control facilities if the SSI effects are considered in the earthquake resistant design of building.

1. Introduction

The research carried out on structural seismic control so far was almost based on the assumption of rigid-foundations, but in reality, the interaction between superstructure and ground is always existent except for constructions directly built upon a well-integrated bedrock, which can be considered approximately as rigid-foundations. Therefore, it is worthy to investigate that whether or not the regular pattern of structural seismic control on rigid-foundations will reflect the real behavior of a building during earthquake. According to references [1][2], the rigidity of ground has an effect on passive seismic control that cannot be neglected and the optimum seismic design can take place only under considerations of the SSI effects as well as ground conditions. Hence, it may be inferred that the SSI effects also have a significant influence on the result of active seismic control. According to references [3][4], in order to achieve the goal of active seismic control there must be a modification in original control arithmetic when the SSI effects are to be considered. And changes needed for the control force are relevant to vibration characteristics of the soil-structure system. The research mentioned above is all based on such assumptions: the superstructure is a linear elastic system of single degree of freedom; the ground is elastic half-space and the input motion is simple harmonic waves. This paper will discuss the active seismic control of structure with emphasis on the effect made by using APC and AARC methods when the SSI effects are considered. The earthquake record is inputted under premise of inelastic structure and a real simulation of actual structural dynamic characteristics.

2. Computational model and method

In the research, the soil-building system is simplified to be two-dimensional, the ground soils are treated as viscoelastic medium which would be a plane strain subject and the lateral boundary of soil mass is treated as a simple boundary. The superstructure is simplified as a plane structure of bar system being composed of variable-section beam elements so that the rigidity difference on different sections of beams or columns caused by differential stress condition can be considered (the details of the rigidity matrix of varying rigidity beam element and the trilinear elasto-plastic constitutive model of reinforced concrete members can be found in references [2][5]

The research was based on the real six-storey frame structure and its sketch drawings of structural computation are shown in fig. 1. The foundation is regarded as a rigid block and the details of building design can be found in reference [2]. The softness and hardness of ground are represented by Vs of shear-wave velocity with which hard soil $Vs = 160H^{0.30}$(m/s) and soft soil $Vs = 120H^{0.30}$(m/s). Here H stands for the depth of soil layers. The depth of bottom boundary of the soil layer was taken as 40m and the damping ratio of the soil mass was taken as 5%. The soil dynamic nonlinear effects essentially soften soils thus the soil nonlinear behavior can be indirectly considered by changing soft-hard conditions of ground.
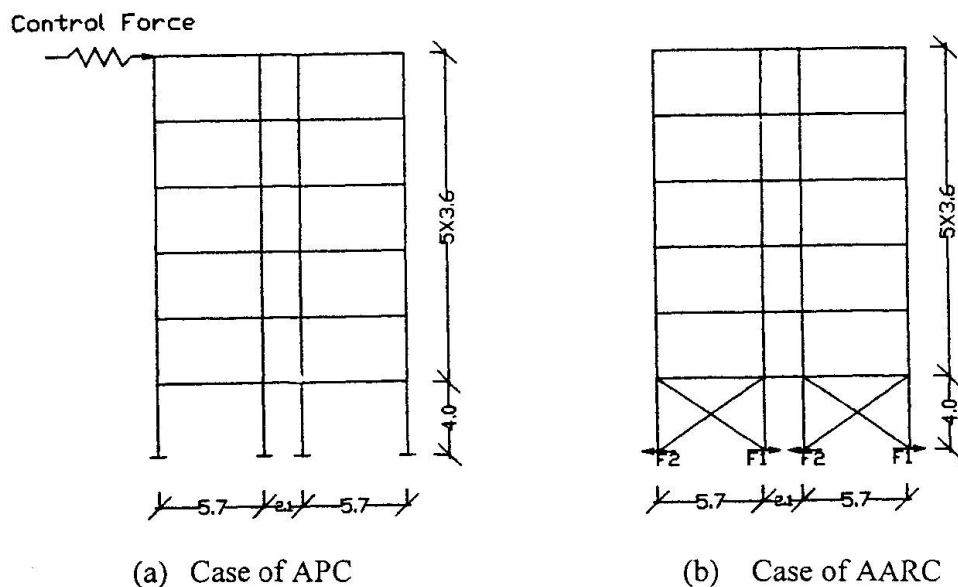

(a) Case of APC   (b) Case of AARC

Figure 1, sketch for computational model of superstructure (unit: m)

The input motion is an El Centro earthquake acceleration record. Taking into account of small, medium and strong earthquakes, the maximum peak value is correspondingly taken as 70, 200 and 400cm/s^2. Under the condition of rigid-foundations the input motion was simply controlled by regulating the value of actual motion proportionally. When the SSI effects are considered, the intensity of input motion determined by the acceleration peak value of the mass center of foundation which is unknown before the numerical analysis. For this reason the value adjustments of the input motion are needed in order to compare with the condition of rigid-foundation assumption.

Any measurements of earthquake response of structure can be easily calculated by solving the dynamic equation of the SSI system using Newmark-β method [6][7]

3. Active Pulse Control (APC) Of Structure Considering SSI Effects

The pulse generator is placed on the top of structure (see fig.1). The control arithmetic adopted is that the direction of the control force generated by the pulse generator is opposite to the relative displacement direction of the top structure and the amount of the control force is equal to the relative displacement of the top structure multiplied by the gain factor.

With the consideration of the SSI effects the earthquake response was analyzed in 27 combined cases on the basis of the small. medium and strong motion: rigid. hard and soft ground: and gain factor being taken respectively as 600. 800 and 1000kN/m. The value of relative displacement under the motion is illustrated in fig. 2 to 4. The illustrations also include results of earthquake response analysis for 9 combined cases of non-control facilities. so they can be compared with the results of the APC. The results show that the earthquake displacement of structure was reduced by the SSI effects. and the softer the ground. the smaller will be the earthquake response. In other words. the softer the ground, the greater will be the earthquake response of superstructure influenced by the SSI effects and the smaller will be the earthquake response of superstructure in comparison with the condition of rigid-foundations. The table 1 shows the maximum value of the APC force needed. In general. the result of active control is better when the gain factor K equals to 800kN/m. In comparison with the APC force under assumption of rigid-foundations. the SSI effects cause the use of less APC force. and the softer the ground. the smaller the control force needed. The APC force needed will become greater when the gain factor K is increased.

Since the amount of the control force is determined by the earthquake displacement response of structure in the APC mothed. thus there are two important meanings to consider the SSI effects during the structural aseismic design. Firstly. as the objective of active seismic control is to confine the earthquake response of superstructure to a certain extent and the SSI effects would lessen the earthquake displacement of structure. so the condition of displacement control will be satisfied automatically without the need of extra active seismic control facilities. Secondly. as the SSI effects greatly reduce the APC force needed. so the power for the APC system would be lowered enormously with which the cost could be cut down.

Table 1   Maximum Control Force Needed

|		For APC (kN)			For AARC (kN)	
gain factor K (kN/m)		600	800	1000	4000	6000
small earthquake	rigid ground	32.0	39.4	53.8	65.2	94.8
	hard ground	20.0	24.6	34.3	53.2	78.6
	soft ground	14.8	18.2	23.9	49.6	71.4
medium earthquake	rigid ground	88.4	112.7	153.8	186.4	270.6
	hard ground	57.3	70.6	98.1	144.8	208.8
	soft ground	42.4	52.1	68.2	141.2	203.4
strong earthquake	rigid ground	174.7	215.5	268.1	334.8	499.8
	hard ground	114.5	141.0	196.0	296.4	426.6
	soft ground	83.6	102.6	132.6	280.8	399.6
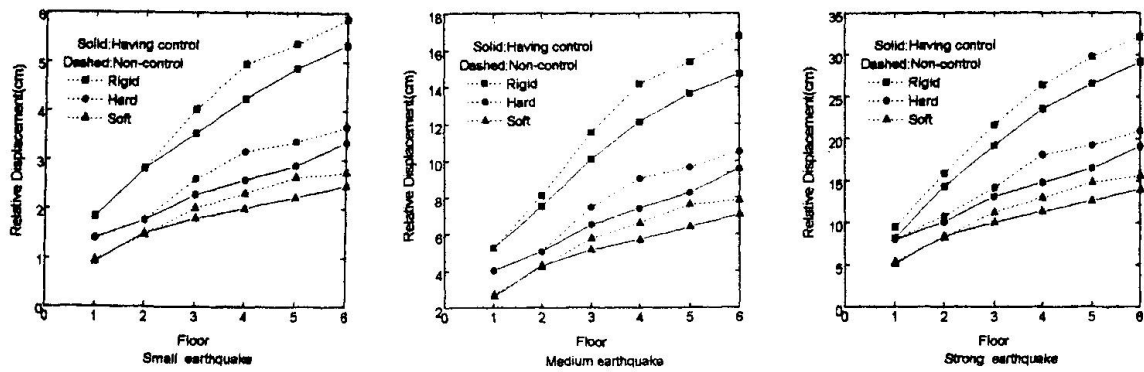
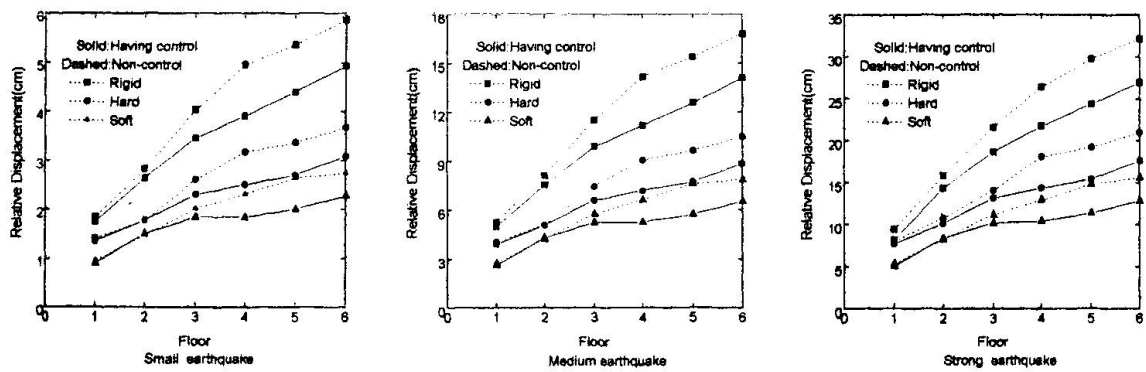Fig.2   Comparison of relative displacement between non-control and APC for K=600 kN/m

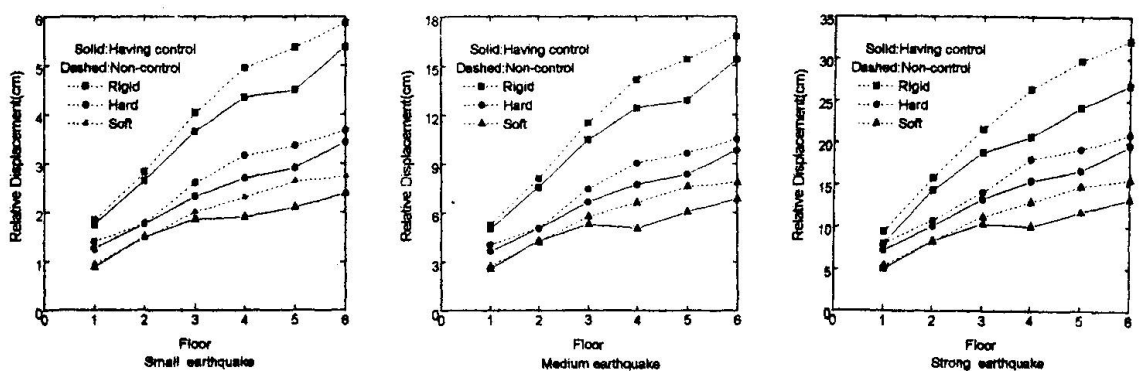Fig.3   Comparison of relative displacement between non-control and APC for K=800 kN/m

Fig.4   Comparison of relative displacement between non-control and APC for K=1000 kN/m

4.   Active Anchor Rope Control (AARC) Considering the SSI Effects

Fig. 1(b) shows the computational model for the AARC. The control force was generated by a servosystem pulling the anchor rope and the amount of the control force equaled to the storey displacement of bottom structure multiplied by the gain factor K. The direction of the control force was determined by the following method: if the displacement of superstructure moves to left, then $F_2 = 0$; if it moves to right, then $F_1 = 0$.

Fig. 5 and 6 show that there are 18 combined cases of storey displacement with the consideration of input motions as the small, medium and strong one; the ground condition as the rigid, hard and soft ground; and the gain factor K taken as 4000 and 6000kN/m. In order to compare with the cases of non-control facilities, the storey displacement of non-control facilities was also given in the figures. Table 1 shows the AARC force needed and the storey displacement of structure lessened by the SSI effects, and the softer the ground, the greater will be the influence caused by the SSI effects. The SSI effects decreased the efficiency of AARC of structure, and the softer the ground, the greater will be the extent decreased. But the SSI effects affected on AARC was limited under the condition of hard ground. That the SSI effects can decrease much control force means the cost could be reduced.
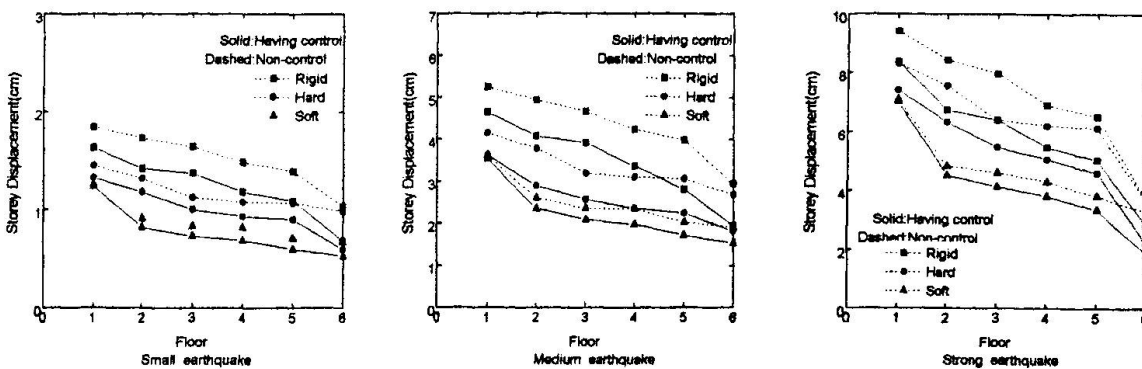

Fig.5   Comparison of storey displacement between non-control and AARC for K=4000 kN/m
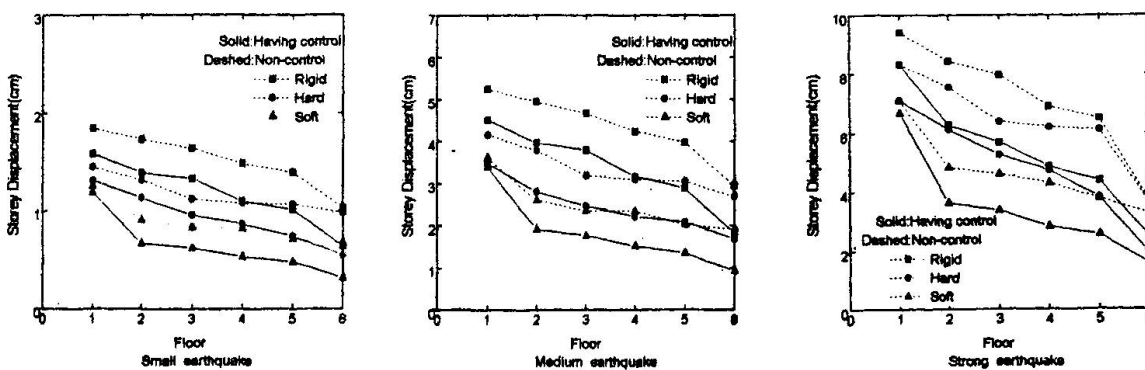

Fig.6   Comparison of storey displacement between non-control and AARC for K=6000 kN/m

5. Conclusion

The active seismic control of inelastic structure under considerations of the SSI effects has been first time analyzed by using the two-dimensional finite element method. After the investigation of the active aseismic control of structure effected by the SSI effects in detail, the conclusion can be reached as follows.

Firstly, since the purpose of active control is to control the earthquake response of structure within a safe extent and for multistorey shear frame structure the SSI effects would significantly decrease the earthquake response of structure, so the actual earthquake displacement of structure would be automatically contented with the purposed degree on rigid-foundation assumption without setting up active seismic control facilities if the SSI effects are to be considered during the structural aseismic design.

Secondly, comparing the two control methods, namely APC and AARC, the APC method needs less control force than the other and its result is quite contented with any type of ground by just regulating the gain factor K to an appropriate value. The result of the AARC on soft ground, however, is not so good, even taking no effect at all. In other words, for multistorey frame structure the earthquake displacement on top storey is controlled in a relatively effective way.

Third, the SSI effects reduce greatly the control force needed for the APC of structure and on hard and soft ground it would be reduced by 1/3 and 1/2 on the frame structure mentioned above, thus, the power consumption is decreased and the cost then could be cut down.

The research is based on specific structure and input earthquake motion, and the ground condition is relatively simple, therefore, it is a initiative and further research is needed.

References

1. Yang D., Chen G. X., and Zai J. M. Study on shock absorbing characteristics of primary and secondary structure. Earthquake Engineering and Engineering Vibration, 1996 (1), 100-109 (in Chinese).
2. Yang D., Chen G. X., and Zai J. M. A study on the effects of SSI on the aseismic characteristics of artificial plastic hinge. Journal of Nanjing Architectural and Civil Engineering Institute, 1997 (2), 15-22 (in Chinese).
3. Wong H. L., Luco J. E. Structural control including soil-structure interaction effects. ASCE, 117 (EM10), 2237-2250.
4. Smith H. A., Wu W. H. and Borja R. L. Structural control considering soil-structure interaction effects, EESD, 23(6), 609-626.
5. Yang D., Ding D. J. and Cao S. Y. A study on the influences of behaviors of new artificial plastic hinge on aseismic character of frame structures. Building Structure, 1994(4), 11-15 (in Chinese).
6. Chen G. X. An integrated system analysis procedure and application software package for analyzing the aseismic behavior of the soil-structure system. Journal of Nanjing Architectural and Civil Engineering Institute, 1992(2), 1-7 (in Chinese).

Experimental Study on Isolation System with Friction Damping

Kazushi OGAWA
Senior Mgr, Bridge Eng. Div.
Kawasaki Heavy Ind. Ltd
Akashi, Hyogo, Japan

Jun-ichi YABE
Senior Officer, Bridge Eng. Div..
Kawasaki Heavy Ind. Ltd
Tokyo, Japan

Tooru NISHIDA
Assist. Mgr, Akashi Techn. Inst.
Kawasaki Heavy Ind. Ltd
Akashi, Hyogo, Japan

Dong-Ho HA
Res. Eng., Bridge Eng. Div.
Kawasaki Heavy Ind. Ltd
Tokyo, Japan

Toshihrio TAMAKI
Staff Officer, Bridge Eng. Div.
Kawasaki Heavy Ind. Ltd
Tokyo, Japan

Fujikazu SAKAI
Dir., Kanto Techn. Inst.
Kawasaki Heavy Ind. Ltd
Noda, Chiba, Japan

Toshio SAITOH
Assist. Mgr , Bridge Eng. Div.
Kawasaki Heavy Ind. Ltd
Akashi, Hyogo, Japan

Summary

The displacement response of seismic-isolated bridges supported on the lead rubber bearings (LRB) or the high damping rubber (HDR) bearings can be very large to great earthquake like the Great Hanshin Earthquake. New type of seismic-isolation system to reduce the displacement response has been developed by the auhors. This new system consist of friction damping bearings, which contain permanent displacement control mechanism by water pressure, and horizontal rubber springs. A series of shaking table experiment had been conducted for the performance verification of a new frictional damping device for seismic isolation of bridge. The excellent energy dissipation effect of friction was identified as the small displacement response with acceptable acceleration response. The comparison of the results of the experiment and the numerical simulation shows the suitability of the simulation.

1. Introduction

The Great Hanshin Earthquake in 1995 caused severe damages on the highway bridges. The seismic isolation systems are used to reduce the response during the earthquake by shifting the natural period of the structure out of the range of dominant earthquake energy and increasing the damping capacity. The isolation systems are recognized as efficient device to reduce the earthquake resopnse. However, the displacement response of the bridges isolated by usual rubber bearings can be 30cm to 70cm to the great earthquake. The design of expansion joints and falling prevention system are difficult to such a large displacement. Therefore the isolation systems with less displacement response are desired. In this paper, the new seismic-isolation system[1,2], the results of measurement of friction elements and the shaking table experiments of the similitude model are discussed. The results of the experiments show the efficiency of the isolators.

2. Isolation system with friction damping

The configuraton of the isolation system with friction damping is shown in Fig. 1. The system consists of the horizontal rubber springs to lengthen the natural period of the bridge structure, and the friction bearings which support the weight of the structure and dissipate the vibration energy by friction. The characteristics of the isolation system with friction damping is as follows.

(a) The vertical load is beared by the friction bearings, traffic vibration does not occur.

(b) The acceleration response of the structure is almost same as the rubber bearings but the displacement response of the structure is well suppressed than by the rubber bearings.

(c) If the residual displacement may occure after the earthquake, the restoration mechanism installed in the device using the water pressure can restore the residual displacement easily.

The isolation system with friction damping can be deformed in horizontal and rotational direction as shown in Fig. 2. The horizontal rubber springs need not bear the vertical force and need not energy dispersion and it is easy to design.
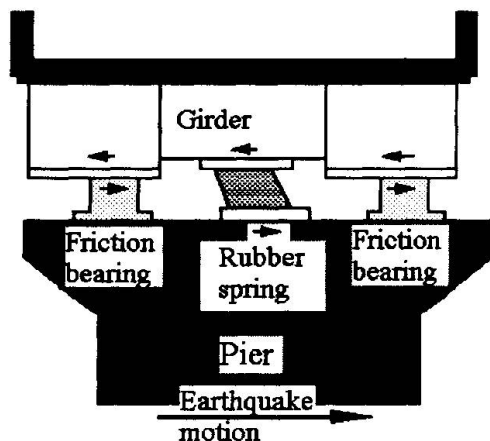

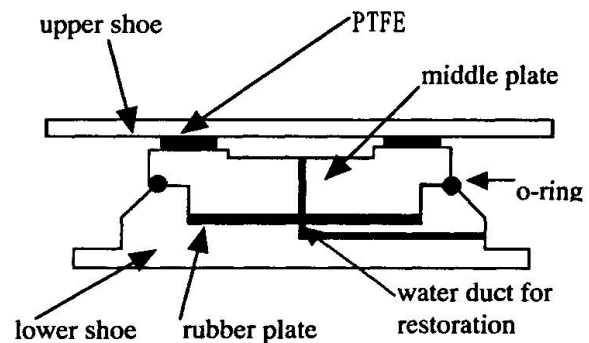*Fig. 1 Configration of isolation system with friction damping*

Fig. 2 Friction Bearing

3. Measurement of friction element

3-1 Experimnetal equipments

As shown in Fig.3, one SUS (stainless steel) plate inserted between the two lower shoes pressed each other is moved by the actuator. The water pressure induced into the cavity in the PTFE (Polytetrafluoroethylene) ring plate reduce the bearing pressure on the ring and the friction force. In this experiment, vertical force, horizontal force, relative displacement and water pressure are measured. The specification of the equipment and the measurement condition are shown in Table 1.
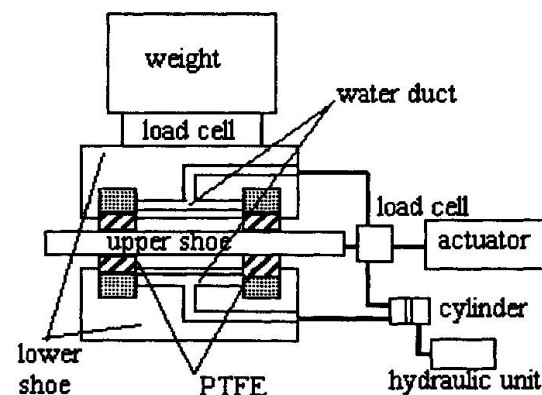

Fig. 3 Equipment for friction measurement

Table 1 Measurement condition

sliding plate	amplitude	135[mm]
	velocity	5~212[mm/s]
PTFE	bearing pressure	9.4,126[MPa]
	area	80[cm^2]
cavity	water pressure	0~58 [MPa]
	area	64[cm^2]

3-2 Results of measurement

The maximum sliding velocity of the PTFE to the SUS are obtained from the time history of the skiding displacement. The coefficients of friction are computed as the ratio of the horizontal force to vertical force. The relation of the friction coefficient and the sliding velocity is shown in Fig. 4. The friction coefficient of PTFE and SUS is small in low velocity region and 0.10 to 0.16 in the region higher than 5cm/sec.

The relation of the sliding velocity and the friction coefficient at each water pressure are shown in Fig. 5. The figure shows the tendency that the higher water pressure makes the friction coefficient smaller in spite of the sliding velocity. Therefore the residual displacement of the bridge can be restored easily by the water pressure. In the case of water pressure higher than 4.6-4.9[Mpa], a little water leakage was observed and the water on the interface of PTFE and SUS reduce the friction coefficient with lubrication effect.
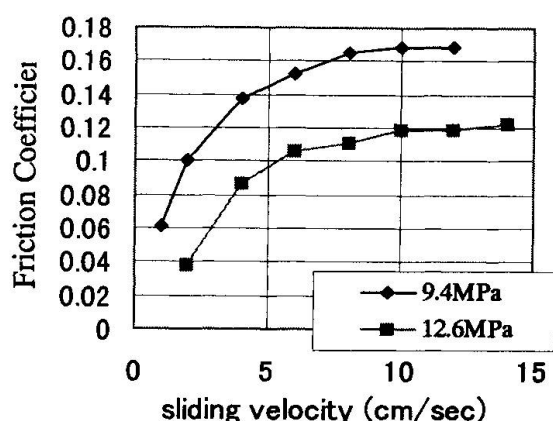

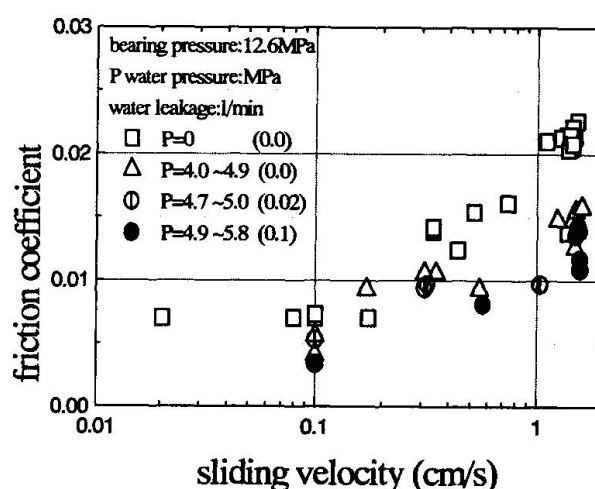*Fig. 4 Velocity and Friction Coefficient*

Fig. 5 Water pressure and Friction Coefficient

4. Shaking table experiment

4-1 Experimental model

The objective bridge of this study is a 5-span continuous steel box-girder with concrete piers as shown in Fig. 6. The shaking table model simulates the dynamic property of the first mode in the logitudinal direction, and of the one span of the girder supported on the isolators above the pier in scale of 1/5. The mass of the model is 10 tons. The natural frequency of the model supported on the horizontal rubber springs is 1.2[Hz] ($\sqrt{5}$ times of the prototype). The dimension of the model is shown in Fig.7 and the photograph of the model on the shaking table in Fig. 8.
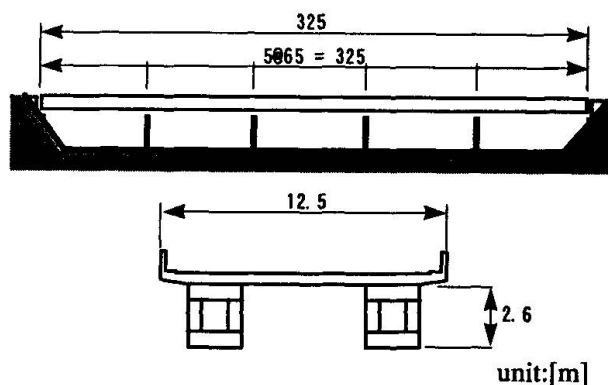

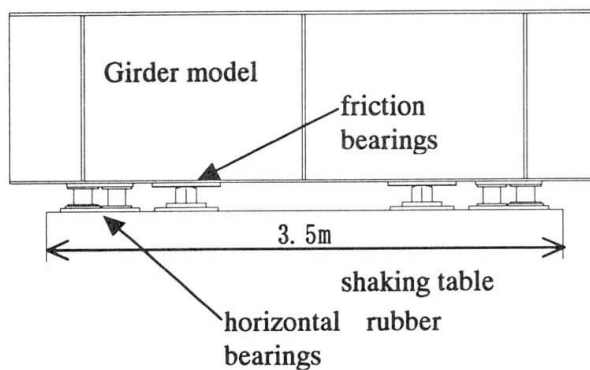*Fig. 6 General view of 5-span continuous steel box-girder bridge*
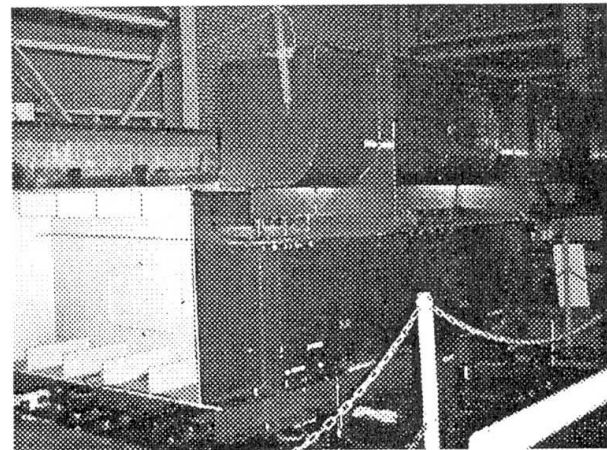
Fig. 7 Model for shaking table experiment

Fig. 8 Model on the shaking table

4-2 Input wave

The sinusoidal waves to investigate the basic characteristics of the model and the earthquake waves to investigate the response of the isolated bridge are used as the input to the shaking table. The earthquake inputs are computed as the response of the pier-girder 2DOF system subjected ground acceleration. The ground motions used for shaking table input are standard time history records for checking design ultimate horizontal strength[3] and the record of the Great Hanshin Earthquake[4]. In Fig. 9 an example of the time history of the acceleration is shown.
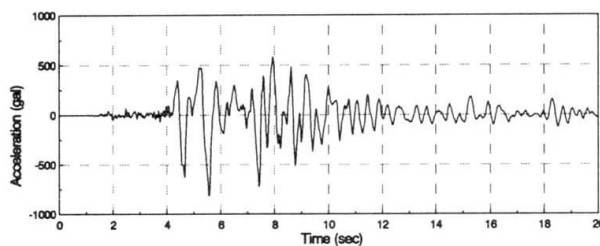
(a) Acceleration at ground
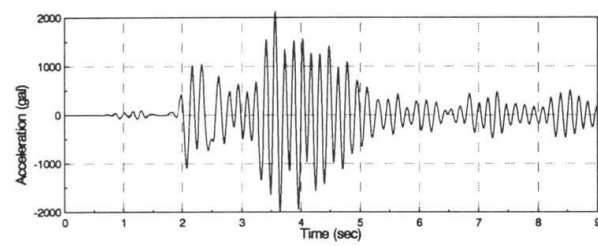
(b) Acceleration at pier

Fig. 9 Input Acceleration (JMA Kobe NS)

4-3 Numerical Simulation

The numerical model of the experimental model is described as a SDOF mechanical vibration system with Coulomb friction as Fig. 12. The equation of motion of the system in Fig.13 is written as follows.

$$\begin{cases} M\ddot{x} + C\dot{x} + Kx = -M\ddot{z} + F_r \\ \quad F_r = -\mu_d Mg \, \mathrm{sgn}(\dot{x}) \end{cases} \quad (1)$$

When

$$\begin{cases} \dot{x} = 0 \quad \text{and} \\ |-M\ddot{z} - C\dot{x} - Kx| \le \mu_s Mg \end{cases} \quad (2)$$
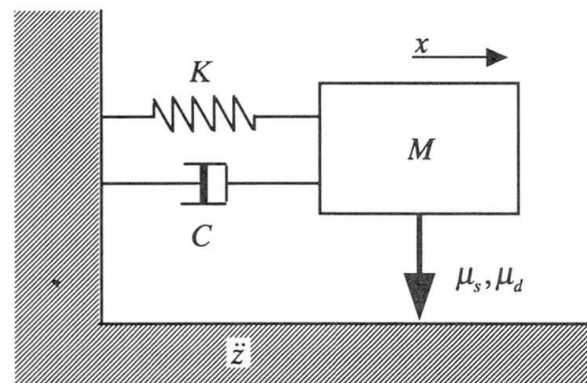
simulation is restarted with the condition

Fig. 10 SDOF simulation model

$\dot{x} = 0$. It means that when the relative velocity is zero and the acting force less than the static friction force, the motion will stop. In the numerical solution procedure of differential equation (1), it is difficult to judge the condition (2) exactly. We evaluated the condition by eq. (3) insetead of eq. (2) using a small value ε and restart with the condition $\dot{x} = 0$.

$$\begin{cases} |\dot{x}| \le \varepsilon \\ |-M\ddot{z} - C\dot{x} - Kx| \le \mu_s Mg \end{cases} \tag{3}$$

Based on the results of measurement of the friction elements, we set the dynamic friction coefficient $\mu_d = 0.14$ and static friction coefficient μ_s as 0.04. Solution scheme by Adams-Gear method with variable time step (0.0001~0.001[sec.]) and $\varepsilon = 10^{-5}$ are used.

4-4 Results of shaking table experiment

a) Harmonic Excitation

Firstly harmonic excitaions of the girder model supported on the horizonal rubber spring are measured. The acceleration amplitude of the shaking table was set to 4, 8, 16, 20 gal. The frequency response is shown in Fig.11. The resonanse frequency changes from 1.42 Hz to 1.26 Hz with increse of input amplitude and it shows that horizontal rubber springs have slightly nonlinear stiffness. The damping ratios were from 0.025 to 0.031 and almost linear.

Next, in the case of girder supported on the friction isolator and horizontal rubber spring, the time history of acceleration is obtained as Fig. 12. In this figure the measurement results (solid line) and results of the numerical simulation (dashed line) are compared. The results of experiment and simulation are in good agreement and the simulation method and parameters are appropriate.

b) Earthquake Excitation

The comparison of time history of the girder on the horizontal rubber spring is shown in Fig.13. In this figure solid line indicates the experimental results and dashed line the simulated results of bi-linear SDOF model. Input wave is based on Kobe JMA NS record (Fig. 9). The difference of the maximum acceleration response is 1.7% and it shows that the property of the horizontal rubber spring is well described by bi-linear model.

The comparison of the time histories of the experiment and the simulation is shown in Fig. 14. This figure shows good agreement of the responses by the shaking table experiment and by the simulation considering Coulomb damping.
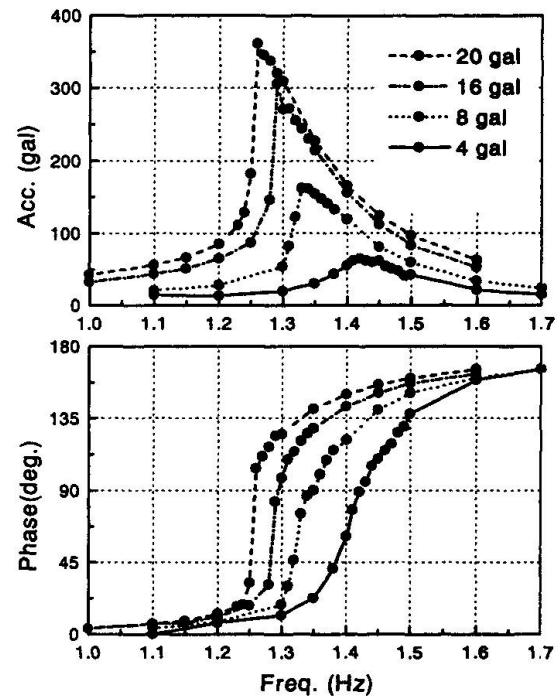
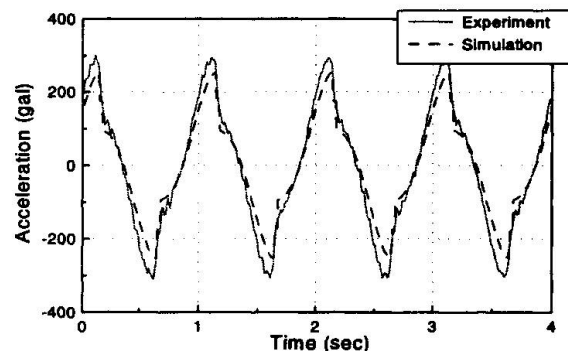Fig.11 Frequency response of girder on rubber spring

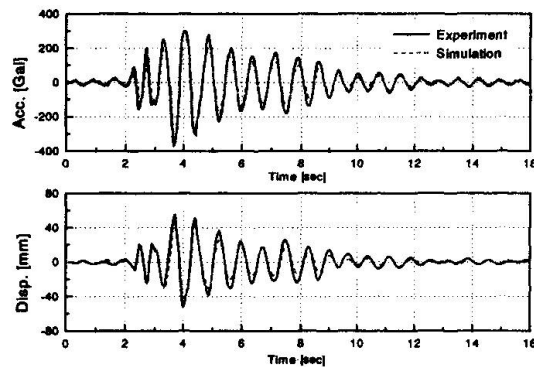Fig. 12 The time history of the gider supported on isolators
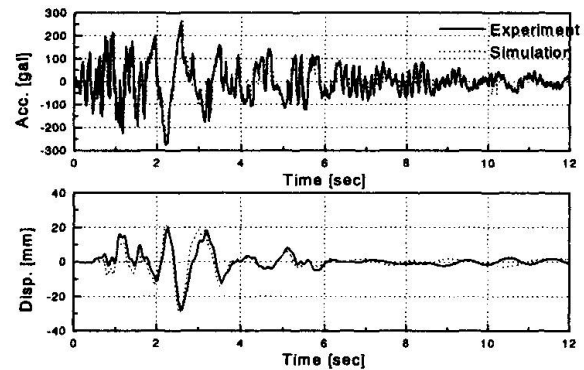
Fig. 13 Response of girder supported on
rubber springs

Fig. 14 Response of girder supported on
isolation system with friction damping

4-5 Comparison of the isolation effect

Based on the results of the shaking table test, we compare the isolation effect of the isolation system with the friction damping and usual rubber isolator by the numerical simulation of the 2DOF model consists of the girder and the pier. In the simulation isolator with the friction damping is treated as a linear spring and Coulomb damping and usual rubber bearing is linear spring and dashpot of 15% of the critical damping. The maximum response of the girder to the earthquake waves are comparerd in the table 2. In this table it is shown that the acceleration response of both isolators are almost same, but the displacement response of the new isolator are much smaller than that of rubber bearings. This shows that the efficiency of the new isolator to suppress the displacement response.

Table 2 The comparison of isolation effect

Input wave	Isolator with Friction		Rubber bearing	
	Acc.	Disp.	Acc.	Disp.
Kaihoku	357	222	377	363
Itajima	373	239	438	415
Tsugaru	389	255	552	532
JMA Kobe	308	170	337	306
JR Takatori	735	604	725	685
Higashi Kobe	403	268	538	528

unit Acc.:gal, Disp. :mm

5. CONCLUSION

The authors discussed the friction measurement and shaking table test of the seismic isolation system with friction damping. The excellent energy dissipation effect of friction was identified as the small displacement response with acceptable acceleration response. A simple simulation with Coulomb damping model was achieved by using the experimental result. The comparison of the results of experiment and numerical simulation shows the suitability of this simulation.

References

(1)Doi Y. et al,"Earthquake isolation of bridge using friction damping shoes", proc. of 1st Colloquim on seismic isolation and control, JSCE 1996.(in Japanese)

(2)Tamaki T. et al, "Experimental study on the seismic isolation system", proc. of JSCE Ann. 1997.(in Japanese)

(3)Civil engineering reserch center, "Temporaly mannual of design method for base-isolated highway bridges ", 1992.(in Japanese)

(4)Japan meteorological agency, "Strong motion record in 1995 Great Hanshin Earthquake", 1995.

Damage Control Design Based on Hysterisis Damping Effect

Masaaki YASUI
Struct. Eng.
Obayashi Corp.
Osaka, Japan

Katuyosi ITAGAKI
Struct. Eng.
Obayashi Corp.
Osaka, Japan

Kiichiro SAITO
Struct. Eng.
Obayashi Corp.
Tokyo, Japan

Sanae FUKUMO
Struct. Eng.
Obayashi Corp.
Osaka, Japan

Summary

Recently, in Japan, remarkable progress has been made in the field of structural response control, after the Hanshin-Awaji Earthquake of 1995 caused many steel structure buildings to fail. This paper reports on the design of a 15-story steel structure building employing two types of hysteretic damper systems. One is composed of a steel bearing wall skirted by boundary beams on either side. The other is composed of a boundary beam passing between two braced mega-columns. In the case of a big earthquake, these boundary beams work as hysteretic dampers through plastic deformation, thereby preventing damage to the main beams and columns bearing vertical loads.

1. Structure Design

1.1 Outline of Structure

The building reported on in this paper is an office building with a 15-story steel structure. The perspective drawing of the building is shown in figure 1. The plan of a typical floor of the building is a rectangle spanning 37.8 by 23.6 meters. The height of the building is 59.3 meters. The plan and section of the building are shown in figure 2 and figure 3. The basic structural system of the building above ground is a moment frame with damper system.

figure 1   A perspective drawing of the building

1 . 2 The mechanism of the damper system

Two types of hysteretic damper systems are applied in the structural design. One consists of the combination of steel shear walls and boundary beams. Henceforth this system will be referred to as the shear wall type. The other consists of the combination of braced mega-columns and boundary beams, and will henceforth be referred to as the brace type.

The shear wall type is made of a steel plate with boundary beams on both sides. The design concept is for the boundary beams to behave as dampers, absorbing seismic energy mainly through plastic deformation in the web, as a result of shear stress. Therefore the web plate is made of low yeild-point steel (LYP235 has a yield strength of about 235 MPa). LYP235 exhibits little deviation of yield strength and good elongation. The architectural advantage of this system is that it allows floor to ceiling openings between boundary beams on both sides of the shear wall.

The brace type is composed of a boundary beam passing between two braced mega-columns, each mega column being composed of two columns joined by cross bracing. In this system the boundary beams dissippate seismic energy mainly through plastic deformation of the flange plates, as a result of bending moment. These beams are made of normal steel material (SM490A, which has a yield strength of about 330 MPa). The design advantage of this system is that floor to ceiling openings can be arranged between boundary beams.
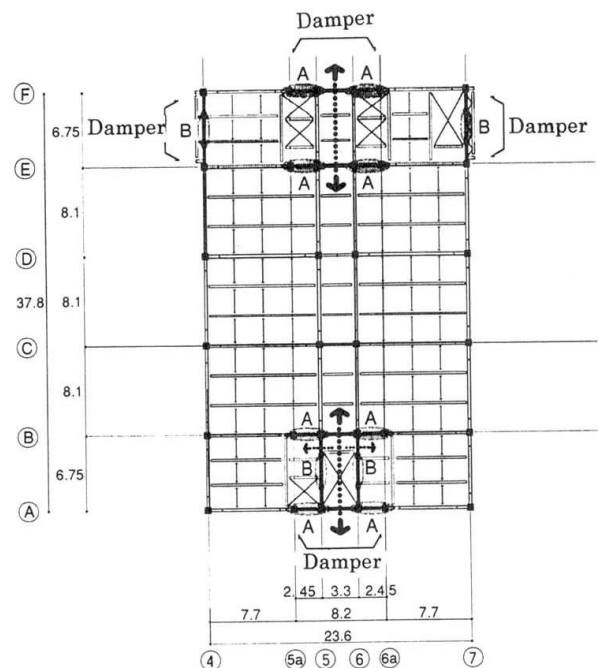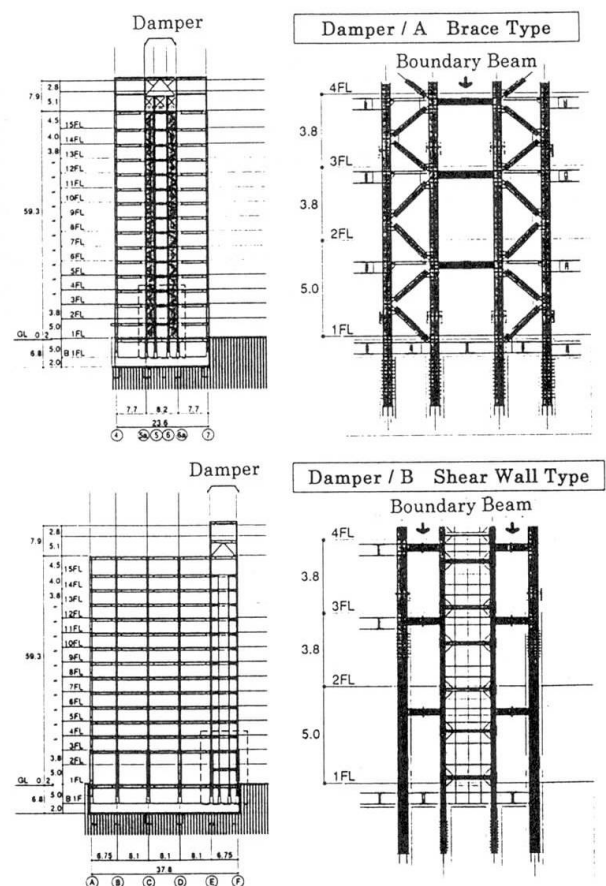

figure 2   The plan of the building

figure 3   The section of the building

1. 3   Strctural Design Concept

The building is designed according to Japanese architectural standards.   In the case of a big earthquake, the boundary beams will work as the hysteretic damper through plastic deformation, thereby preventing damage to main structural members bearing vertical loads. The damper resists about 10% to 50% of the seismic force (average about 30%) at each floor. The target structural performance is shown below.

Table-1   The target structural performance

		Level I (25 cm/s)	Level II (50 cm/s)
Slope by relative storey displacement		under 1/ 200	under 1/ 100
Ductility factor of a general beam		Elastic	under 4.0
Ductility factor of a boundary beam	Shear yield type	Elastic	under 20.0
	Bending yield type	Elastic	under 4.0
Column・brace steel plate shear wall		Elastic	Elastic

2.   Inspection of Damper Effect by Dynamic Analysis
2. 1   Static Elasto-Pastic Analysis

Static elasto-plastic analysis was carried out with a plane frame model.   The skeleton curve of each story is modeled on a tri-linear curve as defined below.   The upper limit of resistance force at each story is defined through the method of virtual work.   The hysteresis characteristic was modeled to Normal Tri-Linear type.

First bending point: point at which any beam at a given story first yields

Second bending point: point at which half of the beams at a given story yield

2. 2 Dynamic Analysis

The response analysis was performed in the cases of the following earthquakes: El Centro 1945 NS, Taft 1952 EW, and Hachinohe 1968 NS, each on both level I (25 cm/s) and level II (50 cm/s). Furthermore, the seismic wave (with a maximum velocity of 85 cm/s) observed during the Hanshin-Awaji Earthquake in 1995 was input for the simulation.   The seismic wave was recorded at the NTT Kobe Building (B3F) located in front of the JR Kobe Station.   The first natural period of the building studied in this report is 1.95 seconds in both directions.   The

result of response analysis is shown in table 2 and figure 4.   The plastic hinges which occured in the building during simulation of the Hanshin-Awaji Earthquake are shown in figure 5. The maximum ductility factor is 2.70 for main beams, 11.5 for boundary beams of shear wall type, and 4.20 for boundary beams of brace type.   It is confirmed that the structure satisfies the target performance through these analyses.   The ductility factor of the typical main beam is smaller than that of a boundary beam.

Table-2 result of earthquake response analysis

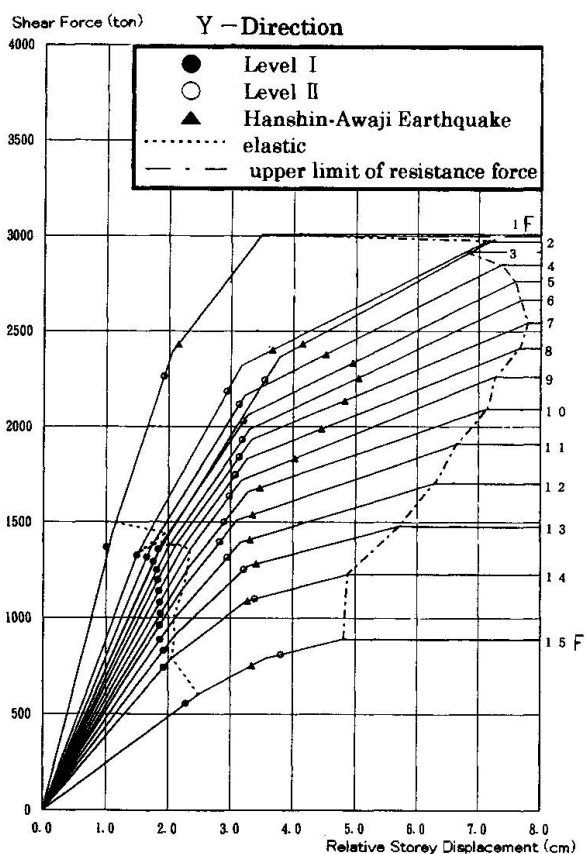|		Level I (25 cm/s)	Level II (50 cm/s)	Hanshin-Awaji Earthquake (85 cm/s)
Slope by relative storey displacement		1/ 196	1/ 102	1/ 74
Ductility factor of a general beam		Elastic	2.05	2.70
Ductility factor of a boundary beam	Shear yield type	Elastic	7.80	11.5
	Bending yield type	Elastic	2.95	4.20
Column · brace steel plate shear wall		Elastic	Elastic	Elastic

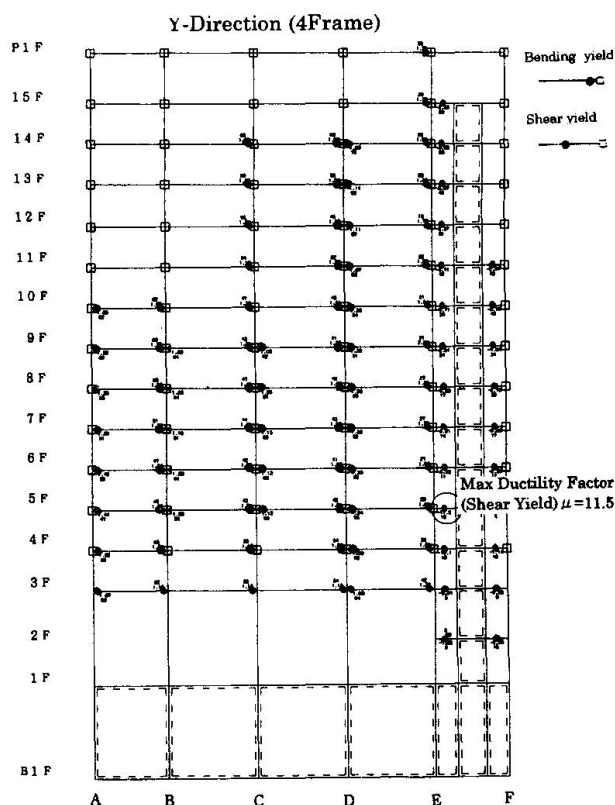figure 4   Skeleton curve and
Result of response analysis

figure 5   The plastic hinges in the building
(Hanshin-Awaji Earthquake)

2. 3 Evaluation of Damping Effect

The total dissipated seismic energy is broken down into viscous damping energy, hysteretic damping energy of damper, and kinematic energy, in order to evaluate the damper's performance.

In the case of the shear wall type damper (long span direction of the building), viscous damping is 2.0%, hysteretic damping of framework is 0.33%, and hysteretic damping of damper is 0.67%.

In the case of the brace type damper (short span direction of the building), viscous damping is 2.0%, hysteretic damping of framework is 0.20%, and hysteretic damping of damper is 0.53%.

M : kinematic energy
C : viscous damping
R : hysteretic damping (frame)
D : hysteretic damping (damper)
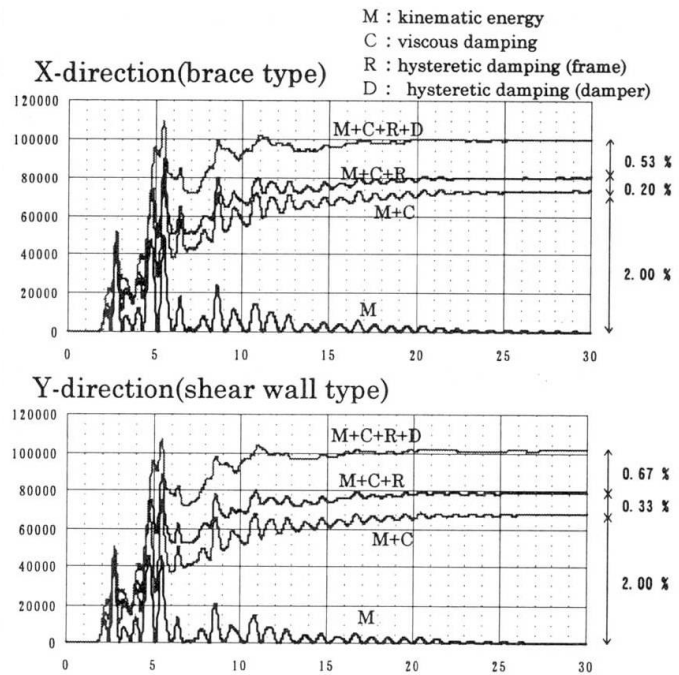
figure 6　Evaluation of Damping Effect

2. 4 FEM Analysis of steel plate shear wall and boundary beam

An FEM analysis of the shear wall system was used to minutely evaluate the stress condition of boundary beams in a state of maximal deformation. Von Mieses stresses for the case of design shearing force and the Hanshin-Awaji Earthquake, respectively, are shown in figure 7. Each member is elastic in the case of design shearing force. The boundary beams yield entirely in the case of the Hanshin-Awaji Earthquake.

figure 7　Result of FEM analysis

3. Conclusion

In general, it is difficult to arrange braces or shear walls in a structural design because they put restriction on the floor plan or to natural lighting.   The damper 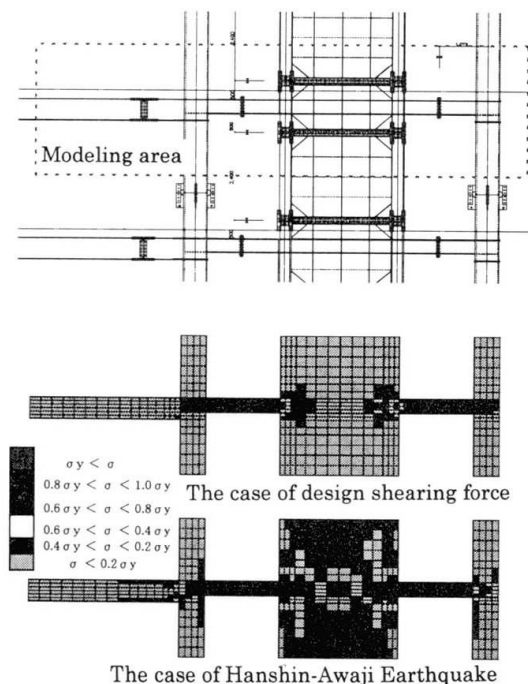systems presented in this paper are, however, of significant advantage to architectural performance, because they can be placed so that openings will accomodate the requirements of a given floor plan. This flexiblility makes these systems widely applicable in the realm of structural response control.

References
1) Kotaro Tanaka, Katuyosi Itagaki, Yosihiko Takahasi : Damage control design based on hysteretic damping effect of 14-story office building with Y-formed brace damper, JSSC annual paper, The 4th volume, pp.396~376, 1996.11
2) Yosihiko Takahasi, Yuuji Sinabe : Empirical research related to a hysteresis characteristic of thin steel plate of shear yield type Architectural Institute of Japan paper selection of structural section, The 494th, pp.107~114, 1997.4

Damage Control Design Based on Attenuation Mechanism by Unbonded Brace

Masanori FUJII
Struct. Eng., Design Dept
Obayashi Corp.
Osaka, Japan

Koutarou TANAKA
Design Team Mgr, Design Dept
Obayashi Corp.
Osaka, Japan

Katuyoshi ITAGAKI
Design Mgr, Design Dept
Obayashi Corp.
Osaka, Japan

Yasuhiro NAKATA
Senior Mgr, Steel Structure Div.
Nippon Steel Corp.
Tokyo, Japan

Summary

This paper shows a damage control design of 19-stories office building by ' Unbonded Brace '. Unbonded brace is a buckling-resistant structural member consisting of steel core members enclosed in a concrete-filled square steel tube. The unbonded braces consisting of steel core member using low yield strength steel become plasticized even at moderate seismic level. At large seismic level, the unbonded braces absorb a large quantity of seismic energy. Moreover, after a large earthquake, unbonded braces can be replaced as required.

Introduction

Since the Hanshin-Awaji Earthquake (1995.1.17) in Japan, studies on seismic energy isolation and damping structures abound and a number of attenuation mechanisms have been proposed. It is noteworthy that the realization of structures with high energy absorption is possible through early plasticization of seismic members (hysteretic damper).

In accordance with this concept, the authors proposed a damping structure. The damage control design for this building is based on attenuation mechanism produced hysteresis damping effect by unbonded brace using low yield strength steel (LYP100 : yield strength $\sigma_y \fallingdotseq 100$ Mpa). This paper outlines the damage control design of a 19-stories office building, which was designed based on attenuation mechanism by unbonded brace and is currently under construction in Osaka.

1. Outline of the Building

Designed building is 19-stories steel structure as shown overall-view in Fig 1. As illustrated Fig 2 and 3, the building consists of main frames with three spans of 9.6 m, and hysteretic dampers (unbonded braces) are situated in common space located at north and south sides. The typical story heights are 3.85 m and 3.8 m, and the height of the building is 85.8 m.

This structure is furthermore characterized by:

(1) mega-structure frame taken advantage of rescue to enhance the hysteresis damping effect by unbonded braces,

(2) concrete filled tubes to enhance the capacity to absorb earthquake energy and the rigidity of 1 and 2 stories with taller height (4.8 m).
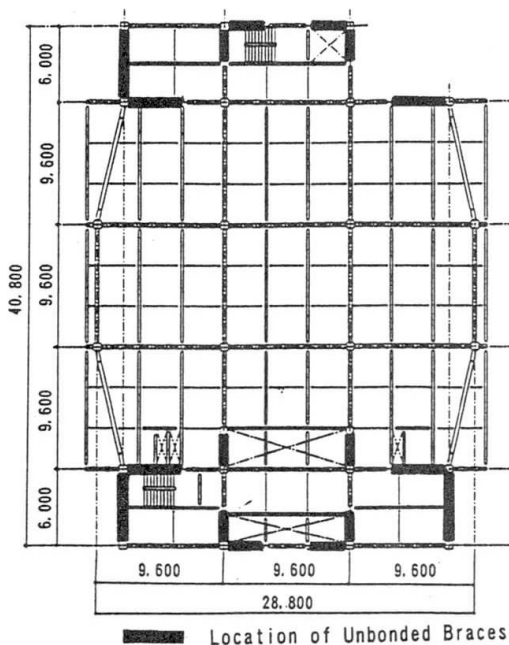

Fig 1   Overall-View

Location of Unbonded Braces

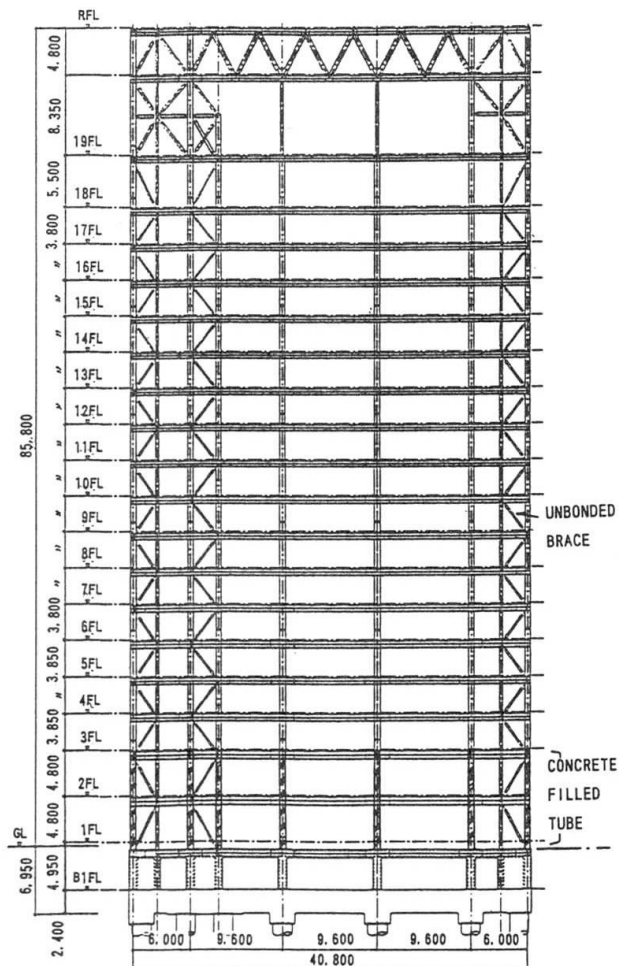Fig 2   Typical Floor Plan

Fig 3   Framing Elevation (N-S dir.)

2. Seismic Design

2.1 Damping Mechanism

'Unbonded brace' is a buckling-resistant structural member consisting of steel core member enclosed in a concrete-filled square steel tube (Fig 4). The steel core member is coated with a non-bonding material, so that no axial force works on the concrete and the steel tube. Consequently, this brace shows stable hysteresises if the yielding load working on the core member is smaller than the buckling load of the steel tube. Besides the stable hysteresis, this brace shows excellent energy absorption. Because the steel core member is made of low yield strength steel (LYP100: $\sigma y \fallingdotseq$ 100 Mpa) and the hysteresis energy of low yield strength steel is much greater than ordinary steel (Fig 5).
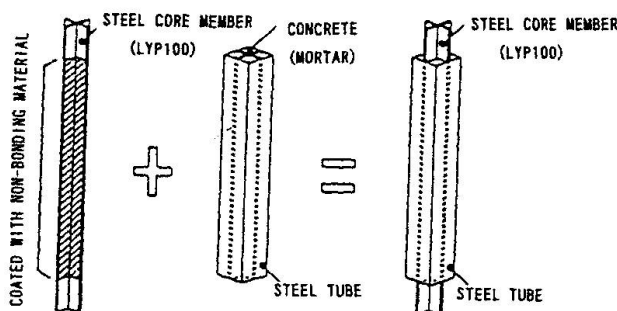

Fig 4   Unbonded Brace
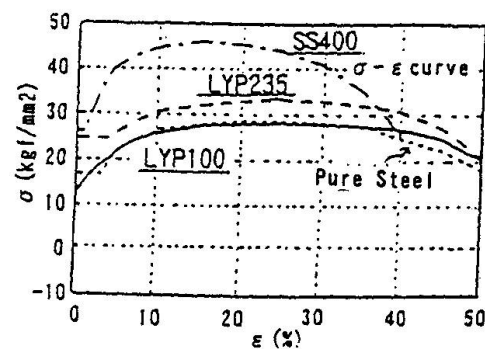
Fig 5   Stress-Strain Curve of
Low Yield Strength Steel (LYP100)

2.2 Design Philosophy

In order to assure earthquake resistance of this structure, it was designed according to the following criteria. Table 1 gives the target values of structural performance obtained from the dynamic response analysis. The axial strength of unbonded braces was designed by aiming at that almost columns and beams are not yielding at seismic level 2 (the ground velocity of 50 kine). At that time, the end joints of unbonded braces are elastic.

Table. 1   Target Values of Structural Performance

Earthquake Ground Velocity	Target Values		
	Story Drift	Ductility Factor of Members	Strain of Members
		Beam	Column	Steel Core Member of Unbonded Brace
25 kine	$\leqq$ 1/200	$\leqq$ 1.0	$\leqq$ 1.0	$\leqq$ 0.005
50 kine	$\leqq$ 1/100	$\leqq$ 2.0	$\leqq$ 1.0	$\leqq$ 0.015

3. Seismic Response Analysis

3.1 Three-Dimensional Static Analysis

A three-dimensional nonlinear static analysis was carried out by the step-by-step method in order to identify the elasto-plastic characteristics of the designed frame, and confirm that the collapse mechanism is determined by flexural yield of beams. As shown in Fig 6 , unbonded braces were analyzed using three divided axial model consisting of ordinary steel (joint) and low yield strength steel (core member). The hysteresis curve of low yield strength steel to harden by repetition was approximated by the result of specimen test (Fig 7) . On the assumption that the floor is rigid, analysis was carried out by applying to the gravity center of each floor incremental load with the same distribution pattern as that of the design shear force.
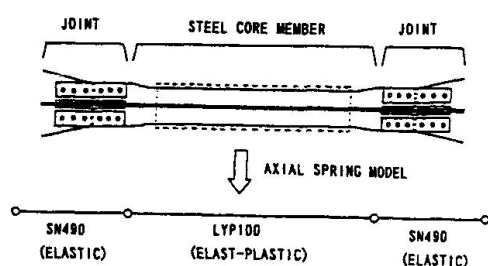

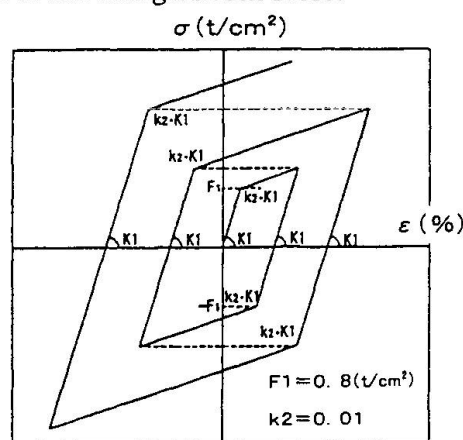Fig 6   Modeling of Unbonded Brace

Fig 7   Hysteresis Curve of
Low Yield Strength Steel (LYP100)

3.2 Time History Seismic Response Analysis

The time history seismic response analysis included: a shear-mode Lumped Mass System Response Analysis which was designed to grasp the response characteristics of the whole structure; a Plane Frame Response Analysis which was designed to grasp the elasto-plastic behavior of structural members (columns, beams, and braces).

In the Lumped Mass System Response Analysis, a model was defined that had 20 mass points (one for each story) on a rigid foundation. Internal viscous damping effect proportional to frequency was assumed, and the damping factor was assumed to be 2% for the first mode frequency. The maximum story drift angle for 25 and 50 kine responses were shown in Table 2   respectively, which are smaller than their respective target values, 1/200 and 1/100.

Table. 2   Maximum Story Drift angle by Lumped Mass System Response Analysis

Ground Velocity	X-direction	Y-direction
25 kine	1/245	1/208
50 kine	1/125	1/117

The Plane Frame Response Analysis was carried out using the wave recorded at the Hanshin-Awaji Earthquake (1995.1.17) with the velocity of 50 kine. Fig 8 shows the distribution of yield hinges produced in Y direction frame. The maximum ductility factor of beams was 1.16, and yield of columns was not observed. The maximum axial stress and strain of unbonded braces was 1.5 (t/cm²), 0.005, respectively (Fig 9 and 10).

For investigating response at largest seismic level, the Plane Frame Response Analysis was carried out using the same wave with the velocity of 75 kine. The maximum ductility factor of beams was 2.6, the maximum strain of the steel core members in unbonded braces was 0.098, and yielding columns was not observed.

From the above results it was confirmed that the response values were within the target range of structural performance. The unbonded braces using low yield strength steel become plasticized even at moderate seismic level. At large seismic level, the unbonded braces absorb a large quantity of seismic energy.

Moreover, numerical analyses on unbonded braces fixed in a frame were made using the non-linear finite element method. The maximum strain of the end in steel core at maximum axial deformation was 0.016. It was confirmed that unbonded braces fixed in a frame can absorb a large quantity of seismic energy.
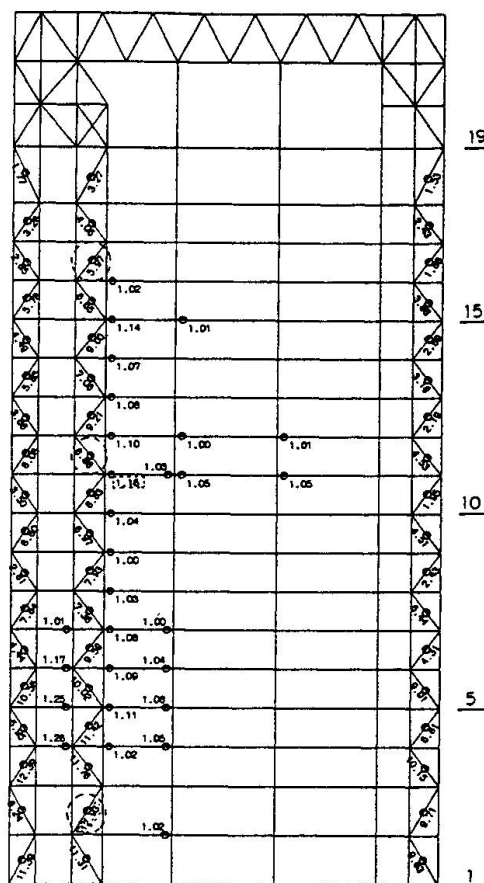

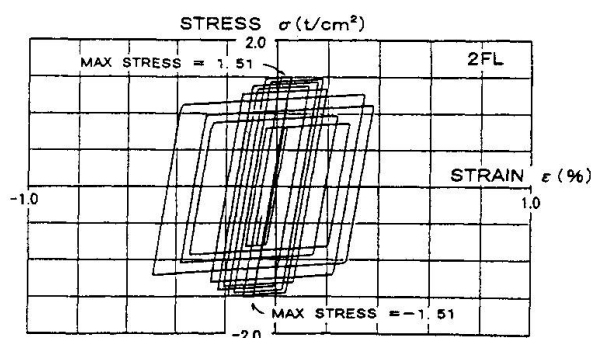Fig 8   Distribution of Plastic Hinges
(Y-dir. 50 kine)

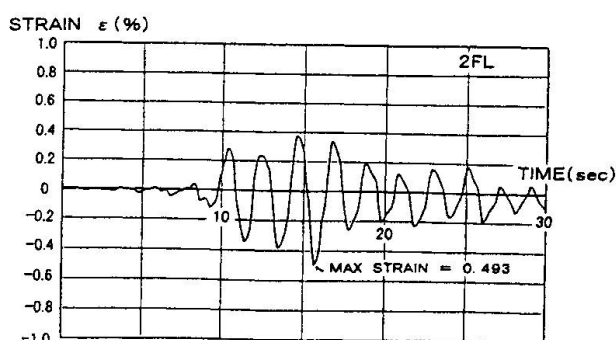Fig 9   Stress-Strain Curve of
Steel Core Member (50 kine)

Fig 10   Strain Time Response of
Steel Core Member (50 kine)

4. Conclusion

The authors designed 19-stories office building which unbonded braces using low yield strength steel was first extensively adopted. According to this attenuation mechanism by unbonded braces, columns and beams was little damaged at large earthquake. Moreover, after a large earthquake, unbonded braces can be replaced as required.

In view of the results of the seismic response analysis, the authors believe that the building designed according to the hysterisis damping effect by unbonded braces using low yield strength steel will prove to be excellent in seismic resistance.

In closing, the authors believe that this damage control design will help to develop 'Structural response control'.

References

1) E.Saeki, Y.Maeda, H.Nakamura, M.Midorikawa, A.Wada: Experimental Study on Practical-Scale Unbonded Braces , J.Struct.Constr.Eng., Architectural Institute of Japan, No.476, pp.149~158,1995.10

2) E.Saeki, M.Sugisawa, T.Yamaguchi, H.Mochizuki, A.Wada: A Study on Low Cycle Fatigue Characteristics of Low Yield Strength Steel , J.Struct.Constr.Eng., Architectural Institute of Japan, No.472 , pp.139~147,1995.6

3) E.Saeki, Y.Maeda, K.Iwamatsu, A.Wada: Analytical Study on Unbonded Braces fixed in A Frame, J.Struct.Constr.Eng., Architectural Institute of Japan, No.489 , pp.95~104,1996.11

4) M.Iwata, Y.Nakata, Y.Maeda, A.Wada: Study on Fatigue Properties of Restoring Dampers Part1,Part2, Summaries of Technical Papers of Annual Meeting Architectural Institute of Japan, StructuresⅢ, pp.733~736,1997.9

Design S-N Curves for Axial Fatigue of Spiral Strands

Mohammed RAOOF
Prof.
Loughborough Univ.
Loughborough, UK

Mohammed Raoof, born 1955, is a graduate of Imperial College where he obtained his BSc, MSc, and PhD. He is the winner of a number of British awards for his research efforts.

Summary

Based on an extensive series of theoretical parametric studies on some very substantial spiral strands with realistic construction details, a new set of S-N curves for predicting the axial fatigue life of spiral strands to first outer (or inner) wire fractures have been proposed. The theoretical model based on which these parametric studies are conducted, has been verified extensively against a very large number of carefully conducted and large-scale test data using specimens with diameters ranging from 25 to 164mm, as produced by different manufacturers and tested by a number of Universities/Research Institutions. The proposed S-N curves are compared with others recommended by API, Chaplin, and Tilly, which are the ones that are currently most commonly referred to and certain shortcomings of previously available recommendations by others are identified.

1. INTRODUCTION

In recent years there has been considerable interest in the tensile fatigue of wire ropes (and spiral strands) for use in both offshore and onshore applications. On the offshore scene, there has been a growing need for longer and stronger elements with larger diameters for use as components in mooring systems for oil exploration, production, and accommodation platforms. As regards onshore structural applications, steel cables are extensively used in bridges and as tension elements for suspended and stayed structures generally.

With the increasing number of available large scale test data for a wide variety of cable constructions, design S-N curves for steel cables have been included in some recent codes of practice in the field of Structural Engineering. One example is API (American Petroleum Institute) recommended S-N curve, another the design S-N curves currently in preparation for the Health and Safety Executive by the Transport Research Laboratories, U.K. Work is also in progress for Eurocode 3. The API and HSE attempts at codifying the S-N curves have taken the form of suggesting lower bound curves to published S-N data with no due attention paid to the specific cable construction details and detrimental termination effects of test specimens which can both be of prime importance.

The present paper presents newly developed S-N curves which take the construction details of large diameter (i.e. realistic) spiral strands into account, and also cater for the effects of end terminations. The proposed S-N curves are based on extensive theoretical parametric studies using a newly proposed model. Finally, the proposed S-N curves are compared with others recommended by API, Chaplin, and Tilly, which are the ones that are currently most commonly referred to, and it is shown that in certain cases, these S-N curves provide unconservative results. As a pre-requisite to this, however, a brief description of the theoretical model follows next, which will, then, enable the reader to better understand (and appreciate) the results presented later.

2. THEORY

Using the orthotropic sheet model (1) it is now possible to obtain reliable estimates of interwire contact forces (and stresses) throughout multi-layered helical strands. Experimental observations suggest that individual wire failures are largely located over the trellis points of interlayer contact and it is now believed that this is as a result of high stress concentration factors in these locations.

Once the maximum effective Von-Mises stress, $\bar{\sigma}'_{max}$, over trellis points of contact, for a given mean axial load on the strand is calculated, the stress concentration factor, K_S, is defined as

$$K_S = \frac{\bar{\sigma}'_{max}}{\bar{\sigma}'} \tag{1}$$

where $\bar{\sigma}'$ is the nominal axial stress in the helical wires which may be calculated using the method developed by Raoof (1).

Raoof (1) deals with the topic of strand axial fatigue at some length. Using the so-obtained values of K_S in conjunction with axial fatigue data on single wires, a theory has been developed which predicts the axial fatigue life of strands (under constant amplitude cyclic loading) from first principles.

For carbon steel wires the fatigue stress-number of cycles plot (S-N curve) possesses an endurance limit, S', below which no damage occurs. Traditionally the magnitude of S' is compared to the ultimate wire strength, S_{ult}: tests on single galvanised wires suggest an approximate value of $S' = 0.27 S_{ult}$. The reduced magnitude of the endurance limit, S_e, which takes interwire contact and fretting plus surface conditions and size effects, etc., into account may be defined as

$$S_e = K_a K_b S' \tag{2}$$

where, $K_b = \dfrac{1}{K_S}$, and K_a is a constant.

The so-obtained values of the parameters S_e, then, are used to produce the S-N curves for fatigue life to first outer (or inner) wire fractures in spiral strands using the S-N curves available in the literature for axial fatigue life of individual wires of a given grade (1).

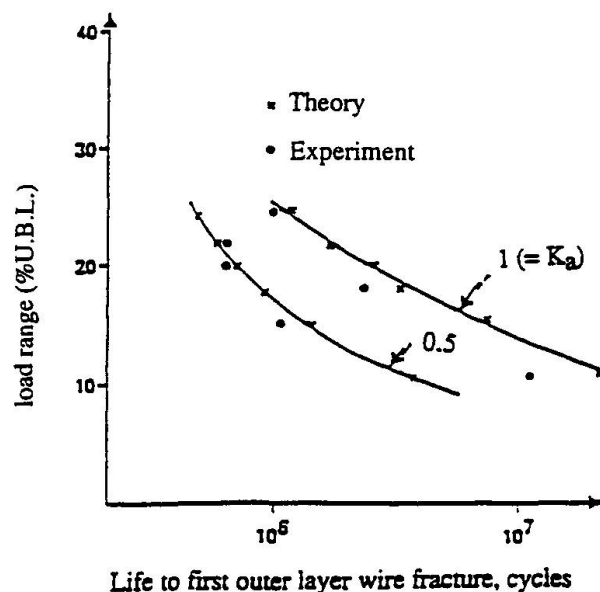

Life to first outer layer wire fracture, cycles

Fig. 1 Axial fatigue of 51mm O.D. strand-comparison of theory and test data.

Fig. 1 compares the theoretical predictions with experimental data for a 51mm diameter spiral strand. The criterion for fatigue initiation has been the occurrence of first wire failure in the outer layer. A fairly significant degree of scatter was found in the experimental data which may be covered by an empirical surface finish factor K_a in the range $0.5 \leq K_a \leq 1.0$. The ultimate tensile strength of the wire material is $S_{ult} = 1640$ N/mm^2. With the strands having epoxy resin end terminations, all the initial wire failures in this strand occurred away from the ends. However, as discussed elsewhere (2), for the end terminations to have no detrimental effects on the wire fractures remote from the ends the minimum length of test specimens must be around 10 lay lengths with the wire fractures occurring within the central region which extends by 2.5 lay lengths on either side of the middle of the test specimen (i.e. within the central portion with a length of 5 lay lengths). It then follows that due to the total length of the tested 51mm O.D. strands being significantly less than 10 lay lengths, even for the wire fractures away from the ends, certain test data points in Fig. 1 have been influenced by the detrimental end effects with the correlations between the theory and such test data suggesting $K_a = 0.5$ as an appropriate factor in the presence of end effects. Otherwise, for wire fractures which happen away from the ends and, in addition, are not influenced by end effects, one may assume $K_a = 1.0$: this, then, provides the reader with an insight into the role of the parameter K_a in the proposed theoretical model.

The theoretical predictions have been supported by a very extensive set of large scale test data relating to spiral strands with diameters equal to 25, 35, 39, 40, 44, 51, 53, 63, 100, 127, and 164mm as produced by different manufacturers and tested by Bridon Ropes, Imperial college, Transport Research Laboratories, and National Engineering Laboratories in U.K., and University of Alberta in Canada, with lay angles within the wide range $11° \leq \alpha \leq 21°$, and wire diameters covering the range 3mm $\leq D \leq 7.10$mm, which very nearly embody the presently adopted manufacturing limits. In all cases, the correlations between the theoretical predictions and such an extensive set of large scale test data has been very encouraging. Space limitations do not allow a full reporting of such good correlations here: these have been reported fully in the references cited elsewhere (3). This, then, provides ample support for the general applicability of the recently proposed theoretical model which can predict both initial outer and/or inner wire breakages with the initial inner wire fractures generally having a lower fatigue life than the outer wires (1).

3. THEORETICAL PARAMETRIC STUDIES

3.1 Background

Recently, Bridon Ropes made the construction details for three realistic types of 127mm diameter spiral strands available to the present author. In particular, three different levels of lay angles (12°, 18° and 24°) were used for designing these strand constructions with each strand having the same lay angle in all its layers and their other geometric factors (such as number and diameters of the helical wires) were kept very nearly the same. As discussed elsewhere (3) following extensive theoretical and experimental work, the lay angle has been found to be the primary factor which controls a number of strand overall structural characteristics with the other geometrical factors being of secondary importance. It should be emphasised that the 12-24 degrees range of presently adopted lay angles cover the full practical range of this parameter as currently used by cable manufacturers. Ref. (3) gives the construction details for 127mm diameter spiral strands used in the following theoretical parametric studies. The assumed Young's modulus for galvanised steel wires $E = 200$ kNmm^{-2} and the Poisson's ratio for wire material $\vartheta = 0.28$. The Ultimate Breaking Load (U.B.L.) of the strands was assumed to be the same, equal to 13510 kN, while tensile ultimate strength of the wire material $S_{ult} = 1520$
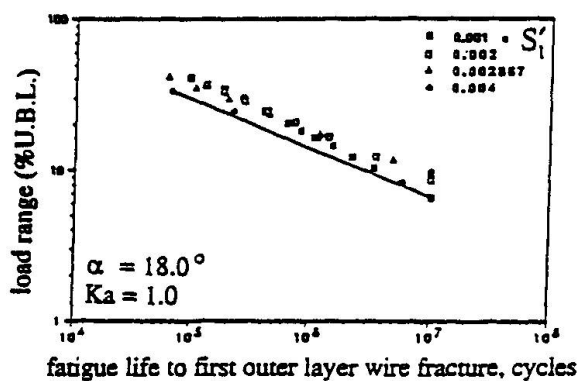
fatigue life to first outer layer wire fracture, cycles

fatigue life, no. of cycles (log scale)

Fig.2

Theoretical effects of changing S'_1 on

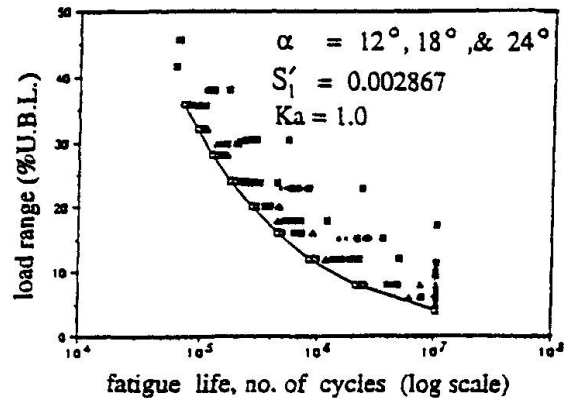axial fatigue life for a given lay angle, α.

Fig.3

Theoretical effects of changing α on axial

fatigue life for a given S'_1 .

Nmm^{-2}.

For the purposes of theoretical parametric studies, four values of strand mean axial strains S'_1 = 0.001, 0.002, 0.002867, and 0.004 were assumed which cover the usual practical working ranges for structural applications. Axial fatigue life was defined as the number of cycles to first wire fracture.

3.2 Design Recommendations

Fig. 2 presents (as a typical example) the plots (in log-log scale) of load range (as a percentage of U.B.L.) against axial fatigue life to first outer layer wire fracture for the 127mm diameter spiral strand with a lay angle of 18 degrees. The assumed value of K_a for this figure is 1.0 - i.e. the initial wire fractures are assumed to happen in the free field and are not affected by end terminations. The plots cover a wide range of $0.001 \leq S'_1 \leq 0.004$. This figure includes a lower bound straight line to all the individual theoretical data points which compared to those in Fig. 3 are found to exhibit a much less degree of scatter. The composite data points in Fig. 3, on the other hand, relate to all the three types of 127mm diameter spiral strands with the lay angles of 12, 18, and 24 degrees and K_a = 1.0 (although, only one value of S'_1 = 0.002867 has been assumed for all the results in this figure and changing the value of S'_1 will cause significantly more degree of scatter in the results). Comparing the scatter of results in Fig. 2 with those in Fig. 3, therefore, strongly suggest the merits in separating the results for each individual value of lay angle: in this way, much more sensible lower bound S-N curves may be obtained with the individual data points relating to each lower-bound S-N curve exhibiting reasonable degrees of scatter. The above exercise may, therefore, be repeated for other cases of practical importance: (a) when K_a = 0.5 -i.e. when individual wire fractures are assumed to be affected by the end terminations; and (b) when the criteria for fatigue failure is changed to that corresponding to the other extreme condition - i.e. when fatigue life is defined as the number of cycles to first wire fracture in the innermost layer of helical wires. In case (b), two separate sets of plots may be obtained: (ii) those with K_a = 1.0; and (ii) another set using K_a = 0.5. Space limitations do not allow presentation of all the plots for cases (a) and (b) in the above, here. Suffice it to say that in all cases, the scatter of the individual theoretical data points (to which a lower-bound S-N curve is added) is similar to those presented in Fig. 2.
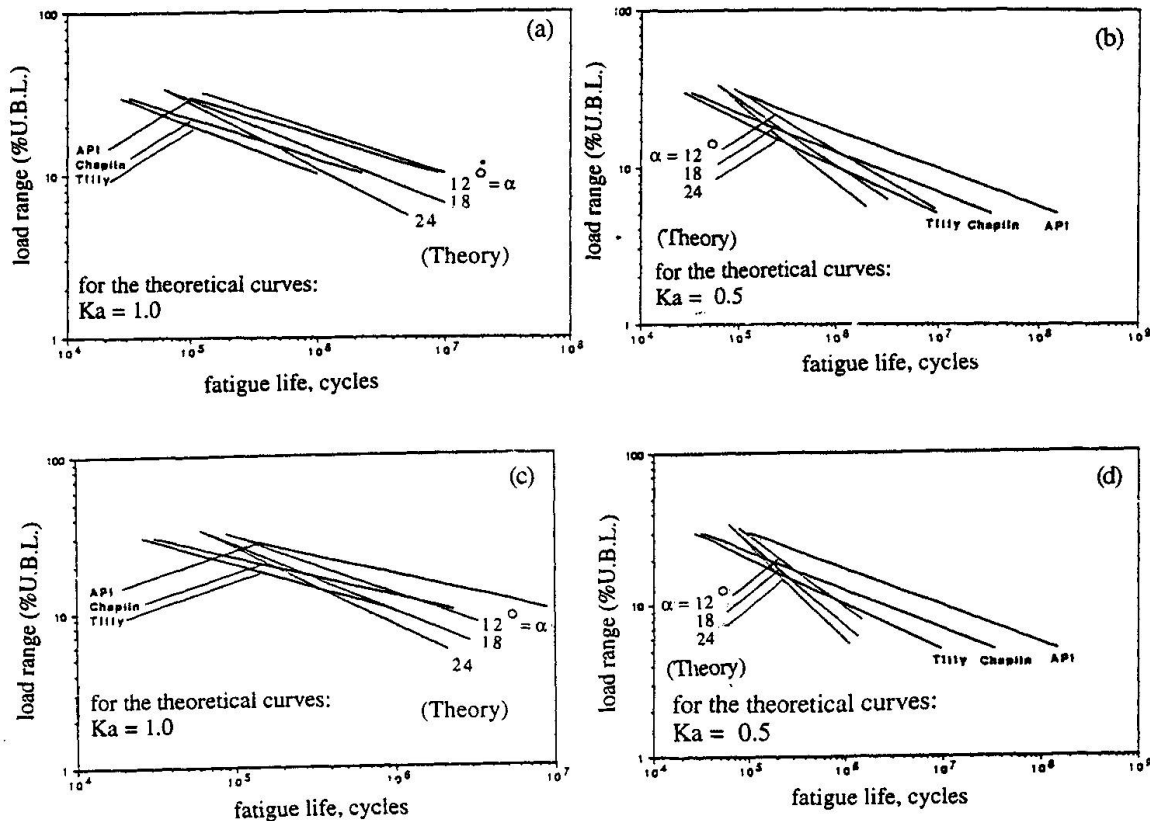
Fig. 4. Comparison of alternative design S-N curves for different values of K_a: (a) and (b) $K_a = 1.0$ and 0.5, respectively, for the fatigue life to first outer layer wire fracture; (c) and (d) $K_a = 1.0$ and 0.5, respectively, for the fatigue life to first wire fracture in the innermost layer.

Figs. 4a-d present all the so-obtained theoretical lower bound S-N curves. Figs. 4a,b correspond to the plots based on K_a values of 1.0 and 0.5, respectively, with the fatigue life defined as number of cycles to first outer layer wire fracture; while in Figs. 4c,d (which, again, assume $K_a = 1.0$ and 0.5, respectively), fatigue life is defined as the number of cycles to first wire breakage in the innermost layer. In each figure, three theoretical lower bound S-N curves corresponding to lay angles of 12, 18, and 24 degrees are presented and, considering that the plots are in log-log scale, the significant influence of lay angle on the axial fatigue life of spiral strands is obvious, with increasing values of lay angles in various layers leading to decreasing magnitudes of fatigue lives (for a given axial load range).

As mentioned previously, the assumed values of strand Ultimate Breaking Load (U.B.L.) and grade of wire for producing the theoretical lower bound S-N curves in Figs 4a-d are 13510kN and 1520 Nmm^{-2}, respectively. However, as discussed at some length elsewhere (3), because the strand axial load range in these plots is non-dimensionalized with respect to U.B.L., all the theoretical lower bound S-N curves are of general applicability irrespective of the magnitude of U.B.L. and grade of wire in practice. Included in Figs. 4a-d are also lower bound empirical S-N curves recommended by API (4), Chaplin (5), and Tilly (6), which are the ones most commonly referred to in the available literature. In producing these purely empirical S-N curves non of these references have differentiated between various types of strand (or, indeed, rope)

constructions used in their experiments. Moreover, different types of failure criterion have been adopted by these references: the failure criteria adopted by Chaplin is number of cycles to total collapse, while Tilly has chosen number of cycles to 5% wire fracture (i.e. life to fatigue initiation). The failure criteria chosen by API is not defined in the code, and there does not seem to be any background literature (available in the public domain) for this recommendation.

The potentially unsafe nature of the previously reported lower bound S-N curves of API, Tilly, and Chaplin for certain (i.e. smaller) levels of axial load range (depending on the magnitude of lay angle), as shown in Figs. 4a-d, is noteworthy. One thing is clear: the API recommended S-N curve can be unconservative for certain practical cases. As regards Tilly's or Chaplin's recommended S-N curves, the situation depends on the failure criteria adopted in practice, and the magnitude of the lay angle for the wires of the strands which are to be used in a given construction. In this context, one should also decide as to whether fatigue failures are to happen at (or in the vicinity) of end terminations or in the free field, away from the ends.

4. CONCLUSIONS

Using extensive theoretical parametric studies (based on a fully verified theoretical model) on some substantial (large diameter) multi-layered spiral strands with realistic construction details and covering the full manufacturing limits of lay angles which are the primary (controlling) parameter, a set of design S-N curves for axial fatigue life prediction of spiral strands are proposed. Unlike previously available and purely empirical S-N curves, the present recommendations cater for the influence of changes in lay angles on the strand axial fatigue life and also can account for the detrimental termination effects. Comparisons are made between the presently recommended design S-N curves and those recommended by others, and the previously available S-N curves are found to suffer from certain shortcomings.

REFERENCES

1. RAOOF, M., "Axial fatigue of Multi-Layered Strands", J. Engrg. Mech., ASCE, Vol.116, No. 10, 1990, 2083-2099.
2. RAOOF, M., and HOBBS, R.E., "Analysis of Axial Fatigue Data for Wire Ropes", Int. J. Fatigue, Vol. 16, Oct., 1994, 493-501.
3. RAOOF, M., "Recommendations Regarding Design of Spiral Stands Against Axial Fatigue Failure", accepted for inclusion in the Proc. of 8th (1998) Int. Offshore and Polar Engrg. Conf., Montreal, May, 1998.
4. API 2FP1 (RP2FP1), API Recommended Practice for Design, Analysis, and Maintenance of Moorings for Floating Production systems, 1992.
5. CHAPLIN, C.R., "Prediction of Offshore Mooring Ropes", Proc. Round Table Conf. on Applications of Wire Rope Endurance Research, OIPEEC, Delft, Netherlands, Sept., 1993, 50-75.
6. TILLY, G.P., "Performance of Bridge Cables", 1st Oleg Kerensky Memorial Conf.held at Queen Elizabeth II Conference Centre, Instn. Structural Engrs., London, U.K., June, 1988, Session 4, 22/4-28/4.
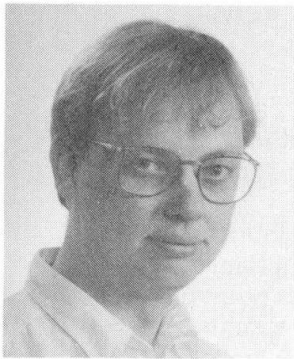
Welded High Strength Low Alloy Steels in Seismic Design
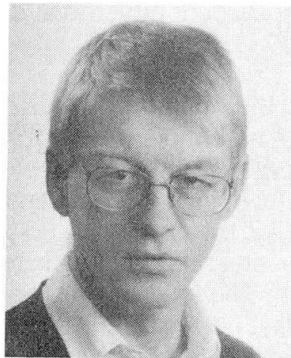
Mikael LORENTZON
Graduate Student
Lulea Univ.
Lulea, Sweden

Kjell ERIKSSON
Assoc. Prof.
Lulea Univ.
Lulea, Sweden

Kjell Eriksson, born in 1941, received his Ph.D. in fracture mechanics in 1975 at the Royal Inst. of Technology, Sweden. His research field is fracture and fatigue of heavy welded steel structures.

Mikael Lorentzon born in 1967, received his M.Sc. degree in mechanical eng. 1992. He is now at Lulea Univ., Div. of Solid Mechanics for research studies in fracture mechanics.

Summary

High strength low alloy steels (HSLA) are frequently used in applications when high strength properties enable weight reduction, e.g. in long span bridges. Results of an experimental investigation show that the HAZ fracture toughness in HSLA depends strongly on the loading rate and temperature. At low and static loading rates ductile behaviour is enhanced and at increased loading rates there is a transition to brittle behaviour. Loading rates that reduce the fracture toughness significantly are frequent in buildings and bridges during a seismic event. This means that surprisingly short fatigue cracks become critical so that dissipative zones may fracture rather than deform and prevent structural collapse.

1. Introduction

In regions of high seismic risk steel structures are usually preferred because of their often superior performance in terms of strength and ductility. Structural ductility is achieved by allowing yielding in selected parts of the structure upon loading beyond a certain level, so-called dissipative zones. During severe seismic events such zones absorb seismic energy through ductile behaviour and hysteresis. Current design methods [1] recommend that connections in dissipative zones shall have sufficient strength to allow yielding of connected parts. In order to ensure this, butt welds or full penetration welds are recommended. It is obvious that this design philosophy assumes that structural elements are free from starting points for fracture, i. e. severe stress concentrators such as sharp defects and fatigue cracks. Despite current seismic design codes, serious failures of steel structures have not ceased to occur. Post-earthquake investigations [2]-[3] have pointed out that welded connections are critical locations for several types of structures. The most typical damages reported from the Kobe earthquake may be summarised as following: 1) fracture of fillet welded joints of beam to column connections, 2) column-to-column with partial joint penetration weld and 3) fillet welded joints of column to through diaphragm. Another interesting observation was that surprisingly short cracks and geometrical discontinuities provided starting points for brittle fracture.

In this work it is assumed that some insight into the cause of some of these failures can be gained through a fracture mechanics approach. Small fabrication defects, e.g. weld undercuts and slag inclusions, are almost always present in welded joints. Fatigue cracks may initiate and grow from such initial defects during normal service. Under normal service loading conditions, short fatigue cracks may exist without seriously affecting the load carrying capacity of a structure. During a seismic event structures are in general subjected to both inertia loads and high loading rates. In a previous investigation [4] it was found that loading rates just above the maximum limit prescribed in the fracture toughness testing standard ASTM E813 [5] significantly affect the fracture toughness of ordinary C-Mn structural steels. In practice that means that shorter cracks become critical and that dissipative zones may fracture rather than deform and absorb energy at increased loading rates.

The observations in [4] raised the question if similar rate effects exists in HSLA steels, particularly in HAZ material. These modern structural steels are frequently used in applications when high strength properties allow weight reduction, e.g. in long span bridges. In this paper the results of an experimental investigation of the fracture toughness of both base and HAZ material of an HSLA steel are presented. The crack driving force in terms of the J-integral [6] is evaluated for an edge cracked beam flange with the finite element method. The loading rates are, from a fracture mechanics point of view, estimated in a simple elastic frame subjected to ground acceleration. The results are discussed in connection to fracture toughness testing requirements in current design codes.

2. Material

The test material comprised both base and HAZ material of an HSLA steel. Two 16 mm plates were joined with a 1/2 V-butt weld. In order to achieve as good toughness properties as possible and to reduce residual stresses welding was performed with multi-run welds and the submerged metal arc process. The chemical composition of the base material is shown in Table 1 and the tensile properties in Table 2. The Charpy-V notch toughness of the base material is typically 30 J at -60 °C.

Table 1. Chemical composition of the base metal (wt %).

C	Mn	P	S	Si	Mo	N	B
.15	1.40	.025	.01	.45	.10	.015	.002

Table 2. Tensile properties of base metal at 20 °C.

ReH [MPa]	R_m [MPa]	A5 [%]
700	780-930	14

Proportional single edge notched bend specimens (SENB) according to ASTM E813 were taken from both base and HAZ material. The notch plane was perpendicular to the rolling direction of the parent material and in the case of HAZ material, parallel to the longitudinal direction of the weld. The HAZ is usually divided into number of subzones depending on the material being welded. Each sub-zone refers to a different type of microstructure and different mechanical properties [7]. In this investigation the interest was focused on the coarse grained material adjacent to the weld metal.

3. Experimental

The quasi-static fracture toughness testing were performed in a servo hydraulic testing machine. Testing was performed at + 20 °C and -30 °C. The low temperature tests were

carried out in a climate chamber. The tests were carried out under displacement control and at different displacement rates. The loading rate in this work is defined as the linear elastic stress intensity rate and is taken as a measure of how fast the crack tip region is loaded. In each test the load and load point displacement signals were recorded with a high speed data acquisition equipment. According to ASTM E813, the critical value of the J-integral, denoted J_c, characterises the onset of crack growth. The J_c values were calculated from the area under the load-displacement curves to the maximum load using the equation for three-point bend specimens:

$$J_c = 2A \ / \ Bb \qquad (1)$$

where A is the area under the load-displacement curve, B specimen thickness and b remaining ligament. A test is considered valid if the specimen thickness meets the requirement:

$$B \geq 25J_c \ / \ \sigma_Y \qquad (2)$$

where σ_Y is the yield strength.

4. Results

For the base metal, no significant loading rate effect on the fracture toughness was observed. This material was ductile at -30 °C over the entire loading rate range investigated. Some typical load versus load point displacement recordings are shown in Fig. 1a. Crack growth was preceded by significant lateral contraction of the material ahead of the crack tip. In all tests pop-in was observed and none of the specimens fractured completely. The obtained fracture toughness is typically greater than 300 kN/m.

The HAZ material showed a brittle behaviour already at low loading rates. From an engineering point of view, all these tests were brittle. The load-displacement curves were almost linear up to the fracture load, Fig. 1b. The fracture toughness was reduced to one third of the fracture toughness at the static loading rate. For the HAZ material, all fracture surfaces showed two distinct regions, a central flat region and a region of shear lips. The central flat region was shiny and faceted and typical for brittle fracture. All tests on the HAZ material at -30 °C are summarised in Fig 2. Only one single test was performed with HAZ material at room temperature and slow loading rate. Surprisingly, this test showed brittle behaviour and the obtained fracture toughness J_c was 86 kN/m.

5. Discussion

5.1 Material behaviour

Modern methods for producing high strength structural steels with yield strength in the range 420-500 MPa are based on thermo-mechanical rolling (TM) and accelerated cooling process. For steels with yield strength in the range 600-960 MPa the QT method (quenching and tempering) is usually preferred. This is in fact the only realistic method to achieve high yield strength without adversing weldability [8]. In practise, both these methods means tightly controlled manufacturing conditions. Welding is in fact a process with quite the opposite effect. As a result of the welding thermal cycle the original micro-structure and properties of the metal in a region close to the weld metal are strongly affected. It is of common knowledge that the microstructure of the grain coarse zone, above all other zones in the HAZ, determine the properties of the weld. In ordinary C-Mn structural steels, low fracture toughness is usually associated with the coarse grained HAZ and the intercritically reheated HAZ. The tests in this investigation show that the fracture toughness at the increased loading rate is further reduced of the order two thirds in the heat affected region. This result was somewhat unexpected considering the excellent properties of the base material. In fact, the fracture toughness values at the increased loading rate are of the same magnitude of order as those of the older C-Mn structural steels reported in [4].

5.2 Application of results

Steel frameworks have many practical applications, such as buildings and bridges. A steel frame essentially consists of beams and columns joined by connections. For the design of structures, the maximum values of relative displacement, relative velocity and absolute acceleration of the response vibration are the most important parameters. Consider for example a simple elastic frame with two columns of height L and with a rigid top beam subjected to a piecewise linear acceleration spectrum, Fig 3. The mass of the top beam is here assumed 8 ton and the total stiffness 900 kN/m. The input load is a total period of 3 s of strong ground motion with a peak ground acceleration of 0.3 g. A numerical solution routine based on the central difference method [9], can be used to solve the equation of motion provided that the time step is considerably smaller than the natural period of the structure. The calculated displacement versus time is shown in Fig. 3. The maximum loading rate in terms of linear elastic stress intensity rate can be estimated from the slope of the displacement curve for some different crack lengths. According to elementary frame analysis, the stress rate at the beam ends can be expressed as

$$\dot\sigma = \frac{\dot M}{W_x} = \frac{6EI}{W_x L^2} \dot u \qquad (3)$$

where E is the elastic modulus, I the moment of area, du/dt the displacement rate and W_x the bending resistance. The linear elastic stress intensity rate for a beam flange with an edge crack is approximately given by

$$\dot K_I = \dot\sigma \sqrt{a\pi} f(a/W) \qquad (4)$$

where a is the crack length, W the flange width and $f(a/W)$ a dimensionless geometry function. With $W_x = 1680$ cm^3, $I = 25\ 166$ cm^4 and $L = 11.2$ m, the maximum loading rate for the case investigated is typically 242-343 MPa$\sqrt{m}$/s for crack lengths 25-50 mm. Even if the response of a real structure is more complicated, this simple example indicates that the loading rate in an elastic frame work is higher than the maximum rate prescribed in current fracture toughness standard (ASTM E813) and within the range of reduced fracture toughness.

5.3 Crack driving force J

The path independent J-integral, is widely used as a criterion in fracture mechanics to determine the onset of crack growth. In this work a finite element model of a beam flange with an edge crack was used to investigate the influence of crack length and stress level on the crack driving force J. For the calculations the finite element program ADINA [10] was employed. The model was composed of 286 eighth-nodes elements and plain strain conditions were adopted. In the crack tip elements 1/r strain singularities were obtained by collapsing the crack side nodes on to one point in the unloaded state. The material model was plastic-multilinear and with data points in general agreement with typical tensile tests on HSLA. About 100 time increments were used through one loading history. The J-integral was calculated for eight contours through the Gauss integration points of the elements surrounding and at different distances from the crack tip.

The calculated value of J versus nominal stress is shown in Fig. 4 for different crack lengths. The lowest fracture toughness data observed in this investigation is marked by a dashed line. Assume that a 25 mm deep fatigue crack exists in a beam element and that the fracture toughness is approximately $J_c \approx 20$ kN/m. That means that a nominal stress level of $\sigma_0/\sigma_Y \approx 0.3$ is sufficient to initiate crack growth. This example shows that already short fatigue cracks are critical and that sufficient fracture toughness is a necessary requirement to achieve global ductility.

6. Conclusions and further work

Further experimental work is necessary to determine the fracture toughness of HAZ material under different welding conditions, loading rates and temperatures. One single test indicated brittle material behaviour already at room temperature. This indication is, if general, of importance for most applications. To determine loading rates from a fracture mechanics point view in some typical structures subjected to ground motion, is another interesting study in prospect. However, based on the findings in this investigation, the following conclusion can be drawn:

> The fracture toughness of HSLA base and HAZ material depends strongly on the loading rate.

> Fracture toughness is strongly reduced at loading rates above the maximum limit prescribed in ASTM E813.

> In common structures loading rates caused by earthquakes often exceed the maximum loading rate prescribed in fracture toughness testing standards.

> A necessary condition for global ductility of structures is sufficient local fracture toughness properties of structural elements and connections.

References

1. Mazzolani F. M. and Piluso V., Theory and Design of Seismic Resistant Steel Frames. St Edmundsbury Press, Bury St Edmunds, Suffolk, 1996.

2. Toyoda M., How Steel Structures Fared in Japan's Great Earth quake. Welding Journal, December 1995.

3. Nakashima S., Kadoya H. and Igarashi S., A Report Concerning Damage to Steel Structures Caused by the Hanshin Earthquake. Nordic Steel Construction Conference, Malmö, Sweden, 1995.

4. Lorentzon M. and Eriksson K., The influence of intermediate loading rates and temperature on the fracture toughness of ordinary carbon manganese structural steels. To appear in Fatigue Fract. Engng Mater. Struct.

5. ASTM E813-89, Standard Test Method for J_{Ic}, a Measure of Fracture Toughness, American Society for Testing and Materials, Philadelphia, 1987.

6. Rice J. R., A Path Independent Integral and the Approximate Analysis of Strain Concentration by Notches and Cracks. Journal of Applied Mechanics, Vol. 35, 1968, 379-386.

7. Easterling K., Introduction to the Physical Metallurgy of Welding, Butterworths, London, 1983.

8. Ahlbom B., Modern Fine Grain High Strength Steels for Structural Applications. Nordic Steel Construction Conference, Malmö, Sweden, 1995.

9. Irvine H. M., Structural dynamics for the practising engineer, Allen & Unwin Ltd, London, UK, 1986.

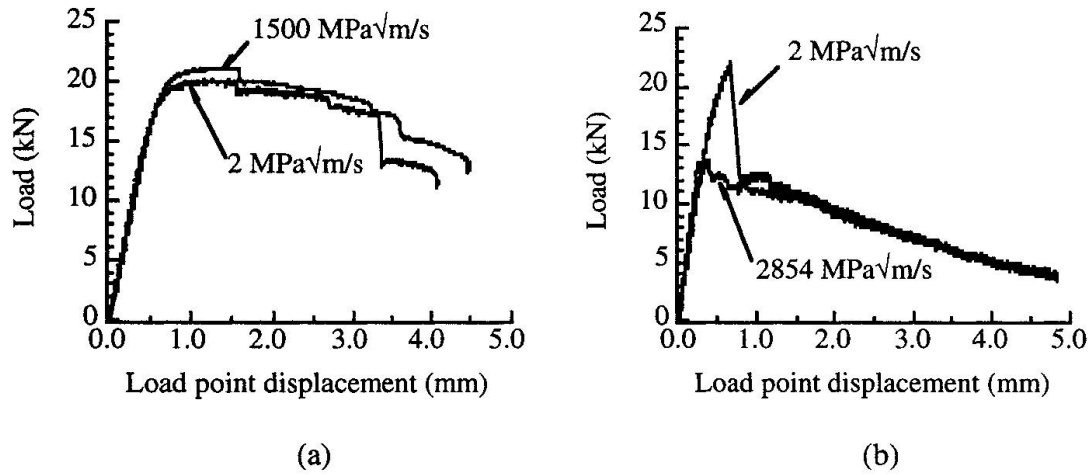10. ADINA, Theory and modelling guide, Report ARD 92-8, 1992, ADINA R&D, Inc., Watertown, MA.

Fig. 1 Load versus load point displacement, a) base metal and b) HAZ material.
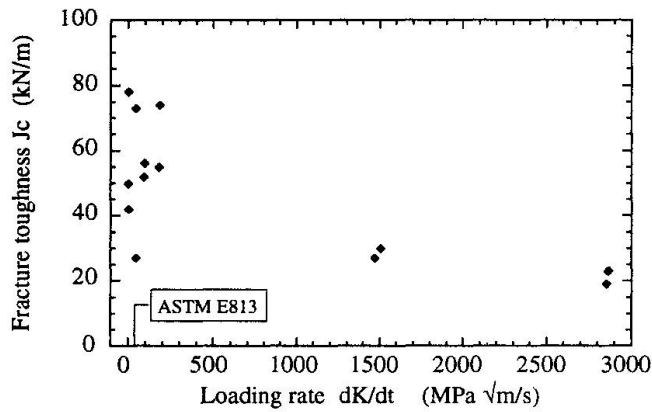

Fig. 2 Influence of loading rate on HAZ fracture toughness at temperature -30 °C.
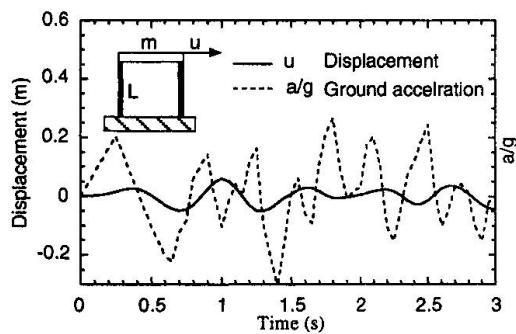

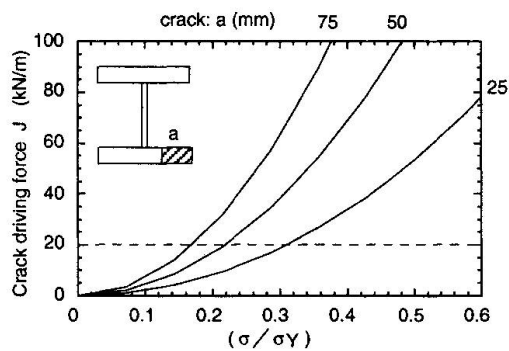*Fig. 3 Response of a simple elastic frame work subjected to ground acceleration.*

Fig. 4 Crack driving force J versus stress for some different crack lengths,

σY = 700 MPa.